

# Assessing Permeability Controls and Flood Risks Related to Urban Impervious Surface Expansion: A Case Study of the Southern Part of Kunming City, China

**Tong Xu**

Yunnan University

**Zhiqiang Xie** (✉ [xzq\\_2019@ynu.edu.cn](mailto:xzq_2019@ynu.edu.cn))

Yunnan University

**Fei Zhao**

Yunnan University

**Yimin Li**

Yunnan University

**Shouquan Yang**

Yunnan University

**Yangbin Zhang**

Yunnan University

**Siqiao Yin**

Yunnan University

**Shi Chen**

Kunming Dianchi Investment Co.,Ltd

**Xuan Li**

Kunming Drainage Facilities Management Co.,Ltd

**Sidong Zhao**

Kunming Drainage Facilities Management Co.,Ltd

**Zhiqun Hou**

Kunming urban underground space planning and Management Office

---

## Research Article

**Keywords:** urbanization, urban flood disaster, flood risk analysis, impervious underlying surface, hydro-hydrodynamic model

**Posted Date:** June 11th, 2021

**DOI:** <https://doi.org/10.21203/rs.3.rs-606230/v1>

**License:**  This work is licensed under a Creative Commons Attribution 4.0 International License.

[Read Full License](#)

---

1 **Assessing permeability controls and flood risks related to urban impervious surface**  
2 **expansion: A case study of the southern part of Kunming City, China**

3  
4 **Tong Xu<sup>1</sup>, Zhiqiang Xie<sup>1</sup>, Fei Zhao<sup>1</sup>, Yimin Li<sup>1</sup>, Shouquan Yang<sup>2</sup>, Yangbin Zhang<sup>2</sup>, Siqiao**  
5 **Yin<sup>2</sup>, Shi Chen<sup>3</sup>, Xuan Li<sup>4</sup>, Sidong Zhao<sup>4</sup>, Zhiqun Hou<sup>5</sup>**

6  
7 **<sup>1</sup> School of Earth Sciences, Yunnan University, Kunming 650504, China**

8 **<sup>2</sup> International Institute of rivers and ecological security, Yunnan University, Kunming**  
9 **650504, China**

10 **<sup>3</sup> Kunming Dianchi Investment Co., Ltd, Kunming 650504, China**

11 **<sup>4</sup> Kunming Drainage Facilities Management Co., Ltd, Kunming 650504, China**

12 **<sup>5</sup> Kunming urban underground space planning and Management Office, Kunming**  
13 **650504, China**

14 **\*Corresponding author: School of Earth Sciences, Yunnan University, Kunming 650504,**  
15 **China (ZQ Xie) [xzq\\_2019@ynu.edu.cn](mailto:xzq_2019@ynu.edu.cn)**

16  
17 **Abstract:** Because of climate change and rapid urbanization, urban impervious underlying  
18 surfaces have expanded, causing Chinese cities to become strongly affected by flood disasters.  
19 Therefore, research on urban flood risks has greatly increased in the past decade, with studies  
20 focusing on reducing the risk of flood disaster. From 2012 to 2020, the impervious underlying  
21 surface has increased, and the permeable underlying surface has decreased annually in  
22 Kunming City. This study was conducted to investigate the impact of continuous changes in the  
23 urban underlying surface on flood disasters in the Runcheng area south of Kunming City from  
24 2012 to 2020. We constructed a two-dimensional flood model to conduct flood simulations and  
25 flood risk analysis for this area. The relationship between the permeability of the underlying  
26 surface and urban flood risk was simulated and analyzed by varying the urban underlying  
27 surface permeability (30%, 35%, 40%, 45%, 50%, 55%, and 60%). The simulation results  
28 indicate that the urban flood risk increased with increases in the impervious underlying surface,  
29 with a threshold permeability of 35%. Once the permeability of the urban underlying surface  
30 decreased to below 35%, the flood risk increased rapidly. We demonstrated the impact of the  
31 urban underlying surface permeability on the risk of urban flood disasters, which is useful for  
32 urban planning decisions and urban flooding risk controls.

33  
34 **Keywords:** urbanization, urban flood disaster, flood risk analysis, impervious underlying  
35 surface, hydro-hydrodynamic model

36  
37 **1. Introduction**

38 In recent years, global warming has increased, extreme weather has occurred more  
39 frequently, and urban flooding has become more likely to occur. With continuous urbanization,  
40 the water surfaces of cities have decreased, and their impervious surfaces have increased.  
41 Increases in the impermeable surfaces reduce the absorption capacity of urban surfaces for  
42 rainwater, shorten the duration of surface runoff formation, and intensify the "Rain Island  
43 Effect". The permeability of underlying surfaces of cities has decreased continuously, such that

44 the urban areas of some cities have permeabilities below 30%. When a rainstorm occurs, the  
45 drainage and infiltration capacities of a city with a low underlying surface permeability are  
46 insufficient to cope with the scale of rainfall, increasing the risk of urban flood disasters. From  
47 1989 to 2018, 3945 major flood disasters occurred worldwide. China, India, the United States,  
48 and Indonesia experienced the most frequent disasters, with a total of ~1200 events. According  
49 to Emergency Events Database statistics, 109 flood disasters occurred in 2018, with a relatively  
50 small number of flood deaths (1995) and victims (12.62 million).

51 Urban flood disasters result in serious population and economic losses. From 2008 to  
52 2010, approximately 137 cities experienced more than three floods, and nearly 58 cities  
53 experienced more than 12 h of disastrous flooding during a single precipitation event from  
54 2008 to 2010 (Liang 2016). On July 21, 2012, a torrential rainstorm occurred in Beijing,  
55 resulting in 79 deaths, the collapse of 10,660 houses, and damage to 163 immovable cultural  
56 relics, with 1.602 million victims, traffic losses of 11.64 billion yuan, congestion, and road  
57 interruptions. In the past five years, more than 300 cities in China have experienced various  
58 degrees of flood disasters characterized by wide ranges, long-term ponding, serious subsequent  
59 impacts on urban development and management, and huge losses of life and property. In  
60 August 2018, Typhoon "Winbia" caused torrential rain on August 18–19 in Shouguang City,  
61 Shandong Province, China. Many villages along the Mihe River in Shouguang City were  
62 flooded, and many buildings, farmland, greenhouses, and breeding farms were affected by the  
63 flood, resulting in heavy losses and causing serious impacts on urban roads and populations  
64 that resulted in economic losses as high as 9.2 billion yuan. Because of rapid urbanization and  
65 the effects of climate change, the frequency of flooding has increased, and the impact of  
66 flooding has become increasingly extensive (Shi 2012; Quan 2014). Rapid urbanization,  
67 increases in the impervious underlying surface, and population growth are the main reasons for  
68 urban flooding in China (Yin et al. 2015), and flood disasters have become a common concern  
69 of the Chinese government and the public.

70 Currently, urban storm water models can be divided into three categories: hydrological  
71 models, hydrodynamic models, and simplified models (Jun et al. 2018; Qi et al. 2021). Each  
72 model has advantages and disadvantages. The Environmental Protection Agency's Storm  
73 Water Management Model (SWMM) is a representative hydrological model but has high data  
74 requirements and limitations. Hydrodynamic models use differential equations to calculate the  
75 flow movement with high accuracy but have a low calculation speed. Other simplified models,  
76 such as the cellular automata (CA) model, have become popular in hydrological modeling  
77 because of their low data requirements and fast computing speeds. For urban flood simulation,  
78 the Infoworks ICM software of HR Wallingford company in the United Kingdom has  
79 significant advantages, as it couples an urban drainage network system model and river  
80 channel model to accurately simulate interactions between the underground drainage network  
81 system and surface water. Moreover, the Infoworks ICM model adopts the of complete solution  
82 method, in which the Wiener equation is used to simulate flow in an open channel, whereas the  
83 Preissmann slot method is used to simulate overload of the open channel. This model can  
84 simulate a variety of complex hydraulic conditions and uses the storage capacity to reflect the  
85 pipe network reserves, so as to avoid incorrect predictions of pipeline overload and flood  
86 disasters.

87 Extensive research on urban flooding has been conducted, and researchers have made  
88 good progress regarding its simulation and control. The concepts of low-impact development  
89 and the "sponge city" have been presented to divert and control urban runoff as to alleviate  
90 urban flooding. Currently, researchers mainly use the SWMM, MIKE software, Infoworks  
91 ICM, and other software to simulate urban flood disasters (Xu et al. 2019; Seenu et al. 2019;  
92 Bisht et al. 2016). Digital city models have been generated based on three-dimensional  
93 hydrodynamic models of digital aerial photogrammetry (Rong et al. 2020). In addition, others  
94 have proposed using the ponding diffusion algorithm (Hou 2020) and two-dimensional (2-D)  
95 inundation analysis algorithm (Huang and Jin 2019) with geographic information system (GIS)  
96 and remote sensing (RS) technology, the SWMM, and effective urban storm inundation  
97 simulations using the distributed hydrological model (Meng et al. 2019). One of the main  
98 challenges in urban flood simulation is the lack of data regarding flood parameters and location  
99 and nature of land cover. Some researchers have used the 2-D hydrodynamic model (Mike  
100 urban) to simulate flooding events and measured parameters including infiltration rate, soil  
101 moisture, and soil texture in the field to fit the model (Hossain anni et al. 2020). Others have  
102 proposed a dynamic impact assessment method for rainstorm and waterlogging based on land  
103 use data (Zhu et al. 2019). In addition, the urban hydrological hydrodynamic coupling model  
104 was established to analyze the uncertainty of the urban flood model based on the generalized  
105 likelihood uncertainty estimation method and shuffled complex evolution Metropolis sampling  
106 algorithm (Liu et al. 2020).

107 Research has also been conducted using urban flood simulations and analyses. For  
108 example, some researchers have used the SWMM to construct urban flood simulation models  
109 based on pipe networks and 2-D surface ponding to study the causes and countermeasures of  
110 coastal urban flooding (Xu et al. 2019). The SWMM has also been used to build multi-level  
111 regulation systems for rainwater runoff in sponge reconstruction communities, and to analyze  
112 the impact of sponge reconstruction on the rainwater regulation ability before and after  
113 reconstruction (Chen et al. 2020). Scenario simulation methods were used to simulate urban  
114 flooding and ponding under designed rainfall conditions (Wang et al. 2020). Furthermore,  
115 comprehensive urban drainage models were built based on the Infoworks ICM, different  
116 measured rainstorms were selected for simulation analysis, and the model was used to simulate  
117 the drainage capacity and ponding depth of a regional drainage network system under  
118 rainstorm scenarios with different return periods (Huang et al. 2017; Wang 2018; Wang and  
119 Zhou 2018), as well as perform analyses based on multi-model coupling (Li et al. 2019; Tao  
120 2017; Geng et al. 2019). In addition, CA has been used to build urban storm flood models (Li et  
121 al. 2020; Wang et al. 2020). For flood risk assessment, a risk assessment index system was  
122 established based on GIS, and analytic hierarchy processes were used to determine the index  
123 weight to assess flood risks (Hu et al. 2017; Chakraborty and Mukhopadhyay 2019).

124 Urban flooding poses a great threat to societal and personal safety annually. Therefore, the  
125 governance of urban flooding is an urgent problem faced by urban development, and its  
126 governance and transformation have become hot topics of current urban research (Kong et al.  
127 2021). In previous studies, six different years (1966, 1971, 1976, 1981, 1986, and 2000) and six  
128 simulated land use scenarios (0%, 20%, 40%, 60%, 80%, and 100% impervious surface areas)  
129 were considered to evaluate the impact of urbanization on changes in urban flood risks in  
130 coupled hydrological and hydraulic models (Feng et al. 2021). The impervious underlying

131 surface was used to explore the process of urbanization (Peng 2016; Yu et al. 2018). In this  
132 study, we mainly investigated the influence of different underlying surface permeabilities on  
133 urban flood disasters using the Infoworks ICM drainage flood model and by controlling the  
134 urban underlying surface permeability, combined with different rainfall conditions. We also  
135 evaluated the influence of urban underlying surface changes on urban flooding risks. This  
136 study provides reference urban underlying surface permeability data for controlling urban  
137 flooding risks.

## 138 **2. Study area and data**

### 139 **2.1 Study area**

140 Kunming is located in Southwest China, in the center of the Yunnan Guizhou Plateau  
141 ( $24^{\circ}23'-26^{\circ}22'$  N,  $102^{\circ}10'-103^{\circ}40'$  E). Dianchi Lake is located to the south and is surrounded  
142 by mountains on three sides and the Dianchi Lake Plain. The maximum E–W distance is 140  
143 km, and the maximum N–S distance is 220 km. Kunming is located in a subtropical zone in  
144 northern latitudes. However, most of the region does not experience severe heat in the summer  
145 or severe cold in the winter, and the region has a typical temperate climate. The overall terrain  
146 is high in the north and low in the south, gradually decreasing in a stepwise pattern. The central  
147 part of the region is uplifted, whereas the eastern and western sides are low-lying. The altitude  
148 ranges from 1500 to 2800 m. The altitude of the city center is ~1891 m. The lake basin is  
149 dominated by karst plateau landforms. By 2019, Kunming had a total area of 21,473 km<sup>2</sup>,  
150 built-up area of 483.52 km<sup>2</sup>, permanent resident population of 6.95 million, urban population  
151 of 5.1152 million, and urbanization rate of 73.6%. The average precipitation in Kunming  
152 during 2019 was 48.6 mm, which was 7.5 mm more than that of the previous year. During the  
153 rainy season, Kunming City experiences serious urban flood disasters that cause major social  
154 and economic losses, as well as environmental disasters, seriously damaging the image of the  
155 city. The study area is in the Runcheng area in the south of the Panlong District, adjacent to  
156 Dianchi Lake. Frequent urban floods have exposed some issues in the urbanization process,  
157 including rapid city development, increasing areas of houses and roads, old and weak drainage  
158 pipeline systems and associated infrastructure, and problems regarding the normal operation  
159 and maintenance capacities of urban underground drainage pipelines. In this study, the current  
160 network system in the main urban section of the southern Runcheng area was selected for  
161 analysis, which has an area of 7.64 km<sup>2</sup> (Fig. 1). The Runcheng area is a typical urban flooding  
162 area. In recent years, serious flood disasters have often occurred in this area.

## 163 **2.2 Data**

### 164 **2.2.1 GIS data**

165 The experimental data were mainly provided by the underground pipeline detection and  
166 Management Office of Kunming City and included geophysical data, rainfall measurements,  
167 RS imagery, digital elevation model data, historical waterlogging location information, and  
168 other data, as shown in Table 1. The original geophysical data included inspection well  
169 coordinates, elevations, pipe diameters, pipe bottom elevations, and pipe top elevations, which

170 were the most recent data (collected in 2018).

### 171 **2.2.2 Image data**

172 The remote sensing (RS) images included satellite imagery of Kunming from 2012, and  
173 2020, which had a resolution of 0.5×0.5 m and was obtained from the Google Earth platform.  
174 RS images can be used for underlying surface analysis, which can be divided into the following  
175 six categories: roads, buildings, green spaces, bare soil, hardened surfaces, and water bodies.  
176 Buildings and hardened surfaces hinder the infiltration of rainwater, whereas the permeability  
177 of green space is generally higher than that of bare soil. Therefore, it is necessary to set  
178 different infiltration rates and other parameters for the different underlying surfaces to produce  
179 more accurate simulation results.

180 The underlying surfaces in the study area are shown in Fig. 2 (a) and (b), which are the  
181 results of RS image analyses of data from 2012 and 2020, respectively. Figure 2 shows that,  
182 with the gradual development and utilization of urban land resources, the yellow bare soil  
183 sections later became buildings and roads. According to the underlying surface results, the  
184 proportion of permeable underlying surfaces gradually decreased from 47% to 31%, from 2012  
185 to 2020, while the proportion of impervious underlying surfaces increased from 53% to 69% (a  
186 16% increase in area), which is an important factor in flood disasters in most cities.

### 187 **2.2.3 Rainfall data**

188 The rainfall data included measured rainfall amounts and rainfall types, which were  
189 generated using the rainstorm intensity formula. Different types of rainfall have different  
190 influences on the underlying surface, making it necessary to select representative rainfall  
191 events. The rainfall data used in this study were collected at Wuda village station in Kunming  
192 on August 16, 2020 (Wuda village station is in the northern part of the study area), at an interval  
193 of 5 min, yielding a total rainfall of 99 mm. In addition, short-term rainfall data were generated  
194 by using the rainstorm intensity formula in Kunming City, with recurrence periods of 1, 2, 3, 5,  
195 and 10 years, respectively. These values were used as the boundary conditions for simulation.

196 The rainstorm model selected for this study was the Chicago rainstorm model (Keifer et al.  
197 1957). A heterogeneous synthetic rainstorm process line model was proposed according to the  
198 relationships between rainfall intensity, duration, and frequency (Chicago rainfall process line  
199 model), which has been widely used. The rainstorm intensity formula is as follows:

$$200 \quad q = \frac{167A_1(1+C \lg P)}{(t+b)^n} \quad (\text{Eq. 1})$$

201 where  $Q$  is rainstorm intensity ( $L/(s \cdot hm^2)$ ),  $A_1$  is the rainfall in different return periods (mm),  $C$   
202 is the rainfall variation parameter,  $P$  is the rainfall return period (a),  $T$  is the rainfall duration  
203 (min), and  $B$  and  $n$  are constants reflecting changes in the designed rainfall intensity over time.  
204 For a specific return period, the molecular  $A_1(1+C \lg P)$  of the rainstorm intensity formula is a  
205 constant, set as  $a$ .

206 The Kunming rainstorm intensity formula (2015 version) was derived from the  
207 Notification of Kunming Dianchi Administration on the Issue of the Kunming rainstorm  
208 intensity formula (2015 version) issued by the Kunming Flood Control and Drought-Relief

209 Headquarters Office of the Kunming Meteorological Bureau (No. 3 of Kunming Qi Lianfa  
210 [2015]). The rainstorm intensity formula for Kunming City is:

$$211 \quad q = \frac{1226.623 \times (1 + 0.958 \lg P)}{(t + 6.714)^{0.648}} \quad (\text{Eq. 2})$$

212 The data used to generate this formula were the minute-scale rainfall data from the  
213 Kunming National Benchmark Climate Observation Station (1981–2014), and are mainly  
214 applicable to the downtown area of Kunming.  
215

### 216 3. Methods

217 In this study, simulation was performed using the hydro-hydrodynamic model, which is a  
218 dynamic wave model used to solve the one-dimensional (1-D) Saint-Venant equations. The  
219 2-D inundation model was based on Triangulated Irregular Network to solve the shallow water  
220 equation using the finite volume method. The Infoworks ICM integrated watershed drainage  
221 system model, which is capable of 1-D and 2-D simulations, has been used widely for drainage  
222 system status assessments, urban flood disaster prediction assessments, controlling urban  
223 rainfall and runoff, and storage design evaluations. Using the 1-D urban drainage pipe network  
224 hydraulic model for the drainage system, 1-D river systems hydraulic model, 2-D city/flooded  
225 river basin flood model for the city water cycle, complete system simulation to achieve the  
226 urban drainage pipe network system model, and river model integration, a more realistic  
227 simulation of the underground drainage pipe network and interactions between the receiving  
228 water body and network can be constructed. The main modules of the model included: a  
229 drainage pipe network hydraulic model (a hydrological module, pipeline hydraulic module,  
230 and sewage volume calculation module), river channel hydraulic model, 2-D urban flood and  
231 inundation model, real-time control module, water quality module, and sustainable structures  
232 module.

233 The hydrological calculation module adopts a distributed model to simulate rainfall runoff  
234 and carries out runoff calculations based on detailed spatial divisions of sub-sets of water areas  
235 and surface compositions with different runoff characteristics. In this study, this module was  
236 used to build and simulate the production and confluence of a subset of the water area. For the  
237 runoff generation model, the Horton model was selected, which involves fewer parameters and  
238 is suitable for small watersheds. For the confluence model, the SWMM nonlinear equation was  
239 selected, which has clear physical concepts and high calculation accuracy:

$$240 \quad \frac{\partial A}{\partial t} + \frac{\partial Q}{\partial x} = 0, \quad (\text{Eq. 3})$$

$$241 \quad \frac{1}{g} \frac{\partial v}{\partial t} + \frac{v}{g} \frac{\partial v}{\partial x} + \frac{\partial z}{\partial x} = -\frac{\tau}{\gamma R}, \quad (\text{Eq. 4})$$

$$242 \quad \frac{\partial h}{\partial t} + \frac{\partial(hv)}{\partial x} + \frac{\partial(hv)}{\partial x} = q_{1D}, \quad (\text{Eq. 5})$$

$$243 \quad \frac{\partial hv}{\partial t} + \frac{\partial}{\partial x} (hv^2 + \frac{gh^2}{2}) + \frac{\partial(huv)}{\partial y} = S_{0,x} - S_{f,x} + q_{1D}v_{1D}, \quad (\text{Eq. 6})$$

244 
$$\frac{\partial hv}{\partial t} + \frac{\partial}{\partial y} (hv^2 + \frac{gh^2}{2}) + \frac{\partial(huv)}{\partial x} = S_{0,y} - S_{f,y} + q_{1D}v_{1D}, \quad (\text{Eq. 7})$$

245 where  $A$  is the area of the water crossing section,  $Q$  is the discharge,  $t$  is the time,  $x$  is the length  
 246 in the runoff direction, and  $v$  is the velocity in the  $x$  direction.  $Z$  is the water level,  $g$  is the  
 247 gravitational acceleration,  $\tau$  is the average shear stress around the wet section,  $\gamma$  is the density of  
 248 water, and  $R$  is the hydraulic radius of the wet section.  $H$  is the water depth,  $u$  is the velocity in  
 249 the  $y$  direction,  $q_{1D}$  is the areal discharge,  $S_{0,x}$  and  $S_{0,y}$  are the slopes in the  $x$  and  $y$  directions,  
 250 respectively,  $S_{f,x}$  and  $S_{f,y}$  are the resistance slopes in the  $x$  and  $y$  directions, respectively, and  $U_{1d}$   
 251 and  $V_{1d}$  are the velocity components of  $Q_{1d}$  in the  $x$  and  $y$  directions, respectively.

252 There are many runoff models, among which the Wallingford fixed runoff model is based  
 253 on the calculation of runoff volumes in the United Kingdom. According to the parameters of  
 254 development density, soil distribution type, and pre-stage humidity of the sub-catchment area,  
 255 the runoff coefficient is predicted by a regression equation. We adopted Horton's empirical  
 256 model of surface permeability, which can generally be expressed as a time-related function.  
 257 Horton's formula is as follows (Abulkadir et al. 2011):

258 
$$f = f_0 + (f_c - f_0) * e^{-kt} \quad (\text{Eq. 8})$$

259 where  $f$  is the infiltration rate (mm/h),  $f_c$  is the initial infiltration rate (mm/h),  $f_0$  is the stable  
 260 infiltration rate or limit infiltration rate,  $K$  is the exponential parameter (1/h), and  $T$  is the  
 261 infiltration time (h).

262 The hydrological calculation module and 1-D drainage system hydraulic calculation  
 263 module were used to build the rainwater system model. The 2-D urban/watershed ground flood  
 264 evolution module was used to simulate and evaluate the surface water.

265 To select experimental parameters, we also measured the infiltration rate of grassland and  
 266 bare land in the study area by performing a double-ring instrument experiment, and calculated  
 267 the attenuation coefficient. The experimental principle of double-loop instrument is to inject  
 268 water into the surface loose rock within a certain hydrogeological boundary to make the  
 269 infiltration water reach a stable level, that is, when the infiltration water per unit time is  
 270 approximately equal, the permeability coefficient ( $S$ ) value can be calculated by using the  
 271 principle of Darcy's law (Hou 2019). Darcy's Law is as follows:

272 
$$S = Q / AI \quad (\text{Eq.9})$$

273 where  $Q$  is steady seepage flow (m<sup>3</sup>/min),  $S$  is the permeability coefficient (M/min),  
 274  $A$  is the inner diameter area of the double-loop (M<sup>2</sup>), and  $I$  is the hydraulic gradient.

### 275 **3.1 Model construction**

276 The 1-D drainage system hydraulic model calculation engine uses the fully solved  
 277 Saint-Venant equation to simulate the flow in pipelines and open channels. The 2-D urban  
 278 flood evolution module combines 1-D and 2-D models in Infoworks ICM software. A 1-D  
 279 model was used to determine where the flood occurred, and then a combined 1-D and 2-D  
 280 model was used to study the flood direction and depth in these areas, which can achieve  
 281 economic efficiency in terms of modeling time and accuracy. In this study, this module was  
 282 applied used to simulate the surface water and analyze the flood risk.

283 The network model, hydraulic model, and hydrological model were constructed based on  
284 the data for the drainage network, underlying surface analysis, and other pre-processing,  
285 respectively, and the sub-models were coupled to form a comprehensive urban flood model.  
286 The rationality of the model was verified by the measured rainfall, and multi-scenario  
287 simulation analysis was carried out in combination with the designed rainstorm under different  
288 working conditions to conduct risk assessment of waterlogging in the pipeline network area.  
289 Construction of the pipe network model included the inspection and correction of basic pipe  
290 network attributes and verification of basic data including manhole coordinates, topological  
291 relationships, pipe diameters, pipe bottom elevations, and pipe top elevations. The data were  
292 derived from the latest pipeline survey data, and the ArcGIS software package (ESRI) was used  
293 to integrate the information and establish the database. The Infoworks ICM model software is  
294 highly coupled to ArcGIS and can directly import ArcGIS data into the model to form the  
295 rainwater pipe network model in the study area. Hydrological models generally include a  
296 runoff generation model and runoff concentration model. The runoff generation model  
297 represents the amount of rainwater runoff on the ground, whereas the runoff concentration  
298 model represents the speed of rainwater runoff. Establishing the hydrological model first  
299 requires the study area to be divided into the sub-catchment areas according to the plot  
300 distribution, terrain, roads, distribution of rainwater pipelines in the community, and relevant  
301 data for catchment area divisions. These data are then combined with the GIS hydrological  
302 analysis method, and the rainwater sub-catchment areas are preliminarily divided, and then  
303 further divided into several sub-catchment areas by using Tyson polygons. The pipe network  
304 catchment area was divided into sewage catchment and rainwater catchment areas. The  
305 underlying surface of the built-up area includes traffic, roads, private houses, residences, green  
306 spaces, and impervious pavement, which can be approximately classified into three categories  
307 (roads, buildings, and green spaces). Therefore, the pipe network catchment area should be  
308 classified according to the different underlying surface conditions. Because sewage is  
309 generated from buildings, whereas roads and green spaces do not produce sewage, the sewage  
310 catchment area was the residential sewage catchment area.

311 All underlying surfaces produce rainwater runoff; however, different underlying surfaces  
312 produce different confluence conditions. According to the distribution of underlying surfaces  
313 in Kunming, the runoff generation and concentration coefficients of six types of runoff surfaces  
314 were set (Table 2). Compared to using the same fixed runoff coefficient for the whole area, this  
315 method can more accurately reflect the runoff characteristics of different catchment areas and  
316 ensure that the simulation results are more accurate and reliable. The runoff generation process  
317 of impervious surfaces is relatively stable, and thus the runoff coefficient method was used to  
318 predict rainwater runoff. According to the technical guide for sponge city construction and  
319 codes for outdoor drainage (2016 Edition) (GB 50014-2006), the road runoff coefficient is 0.9,  
320 roof runoff coefficient is 0.9, and unused land runoff coefficient is 0.45. The runoff generation  
321 process for permeable surfaces is relatively complex. In the rainfall process, the soil infiltration  
322 capacity decreases over time and runoff generation coefficient increases. Therefore, the fixed  
323 runoff coefficient method cannot reasonably simulate the runoff generation process for  
324 permeable surfaces. The Horton runoff generation model was therefore used to simulate the  
325 runoff generation process for permeable surfaces.

326 Model coupling means that the sub-models were coupled to achieve water exchange  
327 among the sub-models. The 1-D hydraulic model was used to simulate the flow movement in  
328 the channels of the pipe network, whereas the 2-D surface model was used to simulate the  
329 overflow evolution of surface water and interaction process between the inspection wells and  
330 surface flooding. This included coupling the surface production and confluence model with the  
331 pipe network confluence model, coupling the pipe network confluence model with the 2-D  
332 surface overflow model, coupling the pipe network confluence model with the channel  
333 confluence model, and coupling the channel confluence model with the 2-D surface overflow  
334 model.

## 336 **3.2 Model calibration and validation**

### 337 **3.2.1 Model calibration**

338 The model was calibrated by inputting the measured data into the model for simulation,  
339 and then comparing the results and actual measurements. After the drainage model was  
340 established, it was necessary to check and revise the model by comparing the simulated data  
341 with the measured data. According to the collected rainfall data and ponding data, the accuracy  
342 of the model was verified by using the measured rainfall data from Wuda village station in the  
343 Runcheng area of Kunming City on August 16, 2020. The beginning time of rainfall was 22:00  
344 h on August 16, and the ending time was 0:00 h on August 18. The measured rainfall curve is  
345 shown in Figure 3. The rainfall gradually increased from around 2:00 h on August 17, reaching  
346 a peak at around 4:00 h, after which it gradually decreased.

347 As shown in Fig. 4, the maximum submerged depth was  $\sim 0.52$  m, whereas the average  
348 submerged depth was  $\sim 0.4$  m. At 4 h after the rainfall began, the underground drainage pipe  
349 gradually filled, and the road surfaces began to accumulate water. The water level peaked at 6 h,  
350 after which the rainfall gradually decreased and water level gradually decreased. However, the  
351 time during which water accumulated occurred later than the peak rainfall time, with a certain  
352 hysteresis.

353 The collected water data were limited and could only be obtained from the Internet, media,  
354 and citizens taking photos to determine the water situation and depth. By investigating network  
355 information and Kunming City news reports, we found that the main flooding point was at the  
356 intersection of Guangfu Road and Qianwei West Road, and that the water depth was  $\sim 40$  cm.  
357 By importing the measured rainfall data from Wuda Village on August 16, 2020, into the model,  
358 the intersection of Guangfu and Qianwei West Roads was selected as the monitoring point in  
359 the operation results. A curve of the flooded depth in this location over time (Fig. 4) and the  
360 flooding scenario in a 2-D plane (Fig. 5a) were obtained. According to comparative analyses,  
361 the results of the model were consistent with the statistical flooding data. The water scenario at  
362 the intersection of Guangfu and Qianwei West Roads (Fig. 5b) was consistent with that of the  
363 collected water data, and the average water depth was  $\sim 0.4$  m, verifying the accuracy of the  
364 model.

### 3.3.2 Parameter calibration

The infiltration rate is defined as the amount of water that infiltrates the soil per unit area and unit time, also known as the infiltration intensity (mm/min or mm/h). The infiltration rate under sufficient water supply conditions is known as the infiltration capacity. Soil infiltration laws are typically described quantitatively by the changes in the infiltration rate or capacity over time. The infiltration rate of dry soil decreases over time under sufficient water supply conditions, known as the infiltration capacity curve or infiltration curve. In the initial infiltration stage, infiltrating water is absorbed by soil particles and fills soil pores. This initial infiltration rate is very high. Over time and with increased seepage, the soil moisture content increases gradually, and the infiltration rate decreases. When the soil pores are full of water and infiltration is generally stable, the infiltration rate is referred to as the steady infiltration capacity or steady infiltration rate. The attenuation process from the initial permeability velocity to the stable permeability is determined by the attenuation coefficient  $K$  in Horton's formula (Eq. 8).

To ensure that the model infiltration rate and other parameters are suitable for local use, six different points were selected in the study area, and soil infiltration rate experiments were carried out by using a double-loop experiment. Table 3 and Table 4 show the records of the measured infiltration rate of two points in the study area and records based on the simulated value of the Horton attenuation coefficient  $K$ , respectively. According to the measured values and Houghton simulation results, the Nash-Sutcliffe efficiency coefficient (NSE) was used to calculate the soil infiltration rate and verify the rationality of the model. In general, NSE values  $>0.7$  indicate a high degree of fit for the model. An NSE coefficient close to 1 indicates a better simulation effect. Nash's formula is as follows:

$$NSE = 1 - \frac{\sum_1^n (Q_0^t - Q_i^t)^2}{\sum_1^n (Q_0^t - Q^-)^2} \quad (\text{Eq. 10})$$

where  $Q_0^t$  and  $Q_i^t$  are the measured and simulated values at time step  $i$ , and  $n$  is the total number of time steps.

Table 5 shows the calculated values of the attenuation coefficients of green land and bare land and their NSE values. When  $k=2$ , the NSE value of green space reached a maximum value of 0.85. When  $k=2.5$ , the maximum NSE value for bare land was 0.77. At this time, the simulated results of the model were most similar to the measured data.

The model was constructed based on real pipe network data, localized parameters, and measured rainfall data, and the actual scenario was restored as much as possible. For pipe network data, only the main municipal road was retained, whereas redundant and insignificant rainwater grates and other small branches on both sides of the road were removed. Localized checking parameters were also adopted in setting the model parameters, and the rainfall data were derived from the measured data. To ensure the authenticity of the model, the running speed of the model was greatly increased.

## 403 4. Results

### 404 4.1 Flood risk analysis

405 According to the Code for Outdoor Drainage Design (GB20014-2006), 2014 edition, the  
406 depth of road water in the "Design Standard for Surface Water" refers to the depth of water at  
407 the lowest elevation of the road surface. When the depth of the water on the road exceeds 15 cm,  
408 the lane may be completely interrupted by the shutdown of motor vehicles. Considering the  
409 safety of pedestrians after increases in water levels, a water depth of 0.5 m was used as another  
410 water level classification. The degree of water accumulation in the central urban area of  
411 Kunming City was divided into three grades: low, medium, and high risks (Table 6).

412 Using the model simulation, rainstorms in the study area with recurrence periods of 1, 2, 3,  
413 5, and 10 years were simulated, and a rainstorm pattern was generated using the rainstorm  
414 intensity formula (Fig. 6). The flood risk areas within the study area were identified for the  
415 different return periods to evaluate the flood risk in the area. As shown in Fig. 7, a higher  
416 rainfall return period is associated with greater rainfall and a greater flood risk.

417 As shown in Fig. 7, the flood risk was expressed visually on the map to determine the  
418 flood risk scenarios for certain locations. Because of factors such as delayed data updates,  
419 underground drainage pipe network data from 2015 are lacking; therefore, the current 2020  
420 pipe network data were adopted for the simulation. As shown in Table 7, 15% of the study area  
421 showed a low risk, 53% of the study area showed a medium risk, and 32% of the study area  
422 showed a high risk. When the risk area proportion is large, flood disasters occur more easily. In  
423 addition, with continuous urbanization, flood risks in other areas increase annually.

### 424 4.2 Variations in flood risk with different underlying surface conditions

425 Because of the lack of imagery of the urban underlying surface from other years, the  
426 proportion of the underlying surface was artificially set in a simulated manner to study the  
427 changes in urban flood risk under different underlying surface conditions. The study area was  
428 generalized into three underlying surfaces: green spaces, buildings, and roads. Different  
429 permeabilities of the underlying surfaces were set using the equal proportion method, and  
430 seven different permeability area percentages were simulated (30%, 35%, 40%, 45%, 50%,  
431 55%, and 60%) for flood disaster inversion. The runoff model was based on the surface  
432 drainages set, with buildings and roads using the fixed runoff coefficient method and a 0.015  
433 confluence parameter. The early damage type was used for the absolute value type. The runoff  
434 coefficient of green spaces used the Horton coefficient, initial permeability was set to 227  
435 mm/h, stable permeability was 110 mm/h, and the Horton attenuation coefficient  $K$  was 2.

436 Figure 8 shows the flood risks for 30–60% surface permeabilities. Areas with risk values  
437 of 0.01–0.30 are low-risk areas, whereas 0.30–0.50 indicates medium-risk areas and risk values  
438 higher than 0.50 indicate high-risk areas. It can be seen from the figure that in the process of  
439 increasing the permeability of underlying surface from 30% to 60%, the area of ponding is  
440 decreasing, and the high-level flood risk is less and less.

441 More specific numerical results can be obtained by statistical analyses of the flood risk  
442 area. The total risk area is equal to the sum of the areas of each risk level. The weight of the  
443 flood risk grade is divided, and the contribution areas of different risk grades (low, medium,

444 and high risk) are obtained by multiplying different flood risk areas by their weight. The  
445 contribution areas of the three different risk grades are then added to obtain the total risk score.  
446 Therefore, after consulting the weight data, 0.02 was selected as the weight of the low-risk area,  
447 0.04 as the weight of the medium risk area, and 0.07 as the weight of the high-risk area. The  
448 risk areas obtained from statistics were multiplied by these values, and then the calculation  
449 results of the three risk levels were added to determine the total risk score, as shown in Table 8.

450 As shown in Fig. 9, the proportion of the flood risk area at different surface permeabilities  
451 indicates that medium-risk areas are significantly larger than high-risk areas, followed by  
452 low-risk areas. Figure 10 shows that for a 30% permeable underlying surface, the total flood  
453 risk area is 261,205 and total risk score evaluation is 29,176. However, for a 60% permeable  
454 underlying surface, the total flood risk area is only 96,931 and total risk score is 10,364. When  
455 the permeability of the underlying surface was varied from 30–60%, the flood risk scores  
456 decreased by 182%, 127%, 92%, 65%, 42%, and 20%, respectively. The change in the  
457 curvature of the underlying surface permeability from 30% to 40% was larger than that of the  
458 other intervals, and the flood risk increased rapidly. Figure 10 shows that every 5% increase in  
459 underlying surface permeability increased the flood risk area score by 2122, 2200, 2440, 2818,  
460 3617, and 5613, respectively, and a breaking point in the rate of increase occurred at the change  
461 from 35% to 30% permeability, at which point the risk increased most rapidly. Thus, once the  
462 underlying surface permeability is lower than 35%, the increasing rate of flood risk increases  
463 sharply. Therefore, the optimal urban underlying surface permeability should be greater than  
464 35%.

## 465 **5. Discussion**

466 In this study, the underlying surface permeability was set using the arithmetic difference  
467 method to simulate changes in the underlying surface during urbanization and invert its  
468 influence on urban flood risk. The infiltration rates of green spaces and bare soil in the southern  
469 area of Kunming City were measured using a double-loop experiment, which localized the  
470 simulation parameters and made the results more accurate to the local scenario. Few  
471 researchers have localized the infiltration rate parameters of Kunming City. In the infiltration  
472 rate experiment, we found that the outer ring of the double-loop instrument did not damage the  
473 surface of the bare soil, and the inner and outer rings should be kept well-sealed, otherwise the  
474 water in the inner ring leaks to the outer ring, artificially causing the measured infiltration rate  
475 of the inner ring to be higher.

476 During modeling and simulations, although the data processing method of the basic pipe  
477 network was simple, time and energy are required. Whether the data processing of the basic  
478 pipe network was appropriate is related to water accumulation after operation of the entire  
479 model. The watershed method also had major influences on model operation, including the  
480 manual partitioning of a subset of the watershed and use of a Voronoi diagram, which led to  
481 large differences. The manual subset of watersheds has many limitations that may lead to no  
482 water and watershed model convergence problems, whereas such issues rarely occurred when  
483 using the Voronoi-derived divisions. The accuracy of the simulation was also largely related to  
484 the parameters used in the model. A major contribution of this experimental study was  
485 obtaining localized parameters using field measurements, and then applying them to the model  
486 to produce more accurate results.

## 487 6. Conclusions

488 In this study, an underground pipe network model constructed using the shallow water  
489 equation was used to simulate changes in the urban flood risk from 2012 to 2020 in the  
490 southern part of the Runcheng District of Kunming City under constantly changing underlying  
491 surfaces. We also analyzed the relationship between urban flooding and the underlying surface  
492 permeability during urbanization. We found that the underlying surface permeability was an  
493 important factor affecting urban flooding, and that the optimal urban underlying surface  
494 permeability is >35%. The underlying surface permeability should be maintained above 30%  
495 as the flood risk rate will increase rapidly once urban permeability is lower than 35%, resulting  
496 in the intensification of urban flooding.

497 The influences of different rain types on flooding with the same underlying surface  
498 permeability, as well as the influence of different underlying surfaces with the same rainfall  
499 type on flooding, can be analyzed. In addition, the influence of the underlying surface on  
500 flooding with the evolution of urban construction can be assessed. Although it is accepted that  
501 urban underlying surfaces can aggravate flooding, the specific impacts are not completely clear.  
502 Based on the simulation of historical rainfall conditions, urban flood disasters over many years  
503 can be compared, the formation of water accumulation locations can be determined, and  
504 relationship between the changes in green land rate and floor area ratio and changes in water  
505 accumulation can be analyzed. Such analyses can reflect the influence of the underlying  
506 surface on flooding caused by the evolution of urban construction. By simulating underlying  
507 surface ratio conditions, the water accumulation degree of different underlying surfaces in  
508 daily rainfall conditions can be compared. Combined with the localization parameters from  
509 Kunming City and combined analytical results of various conditions, simulations can provide  
510 suggestions and help control plot ratios and green land rates in urban development.

511

### 512 **Declarations**

513 **Funding** This study was supported by the National Natural Science and technology  
514 foundation of the people's Republic of China (NSFC) project: Research on thematic map  
515 information model and multiple expression based on full information theory (Grant  
516 No.41961064), and the Ministry of housing and urban rural development of the people's  
517 Republic of China (MOHURD) 2017 Science and technology project: Research on Evaluation  
518 of safe operation capacity of important urban underground pipelines (Grant No.2017-k4-009).

519 **Conflicts of interest** No conflict of interest.

520 **Acknowledgements** Thanks for the research support provided by Kunming urban  
521 underground space planning and Management Office and Kunming Drainage Facilities  
522 Management Co., Ltd.

523

## 524 7. References

525 Abulkadir A, Wuddivira MN, Abdu N et al (2011) Use of Horton infiltration model in  
526 estimating infiltration characteristics of an Alfisol in the Northern Guinea Savanna of  
527 Nigeria. J Agric Sci Technol 6:925–931.

528 Bisht DS, Chatterjee C, Kalakoti S, Upadhyay P, Sahoo M, Panda A (2016) Modeling urban  
529 floods and drainage using SWMM and MIKE URBAN: a case study. *Nat Hazards*  
530 84(2):749-776. <https://doi.org/10.1007/s11069-016-2455-1>

531 Chakraborty S, Mukhopadhyay S (2019) Assessing flood risk using analytical hierarchy proce  
532 ss (AHP) and geographical information system (GIS): application in Coochbehar district  
533 of West Bengal, India. *Nat Hazards* 99(1):247-274. <https://doi.org/10.1007/s11069-019-03737-7>

534

535 Chen T, Xia MM, Liu YP, Che AW (2020) Regulation of stormwater runoff in sponge  
536 reconstructed community based on SWMM. *China Water & Wastewater* 36(11):103-111.

537 Emergency Events Database (2020). (Retrieved November 10, 2020, from [https://www.emdat.](https://www.emdat.be)  
538 [be](https://www.emdat.be))

539 Feng B, Zhang Y, Bourke R (2021) Urbanization impacts on flood risks based on urban growt  
540 h data and coupled flood models. *Nat Hazards* 106(1):613-627. <https://doi.org/10.1007/s11069-020-04480-0>

541

542 Geng Y, Zheng X, Wang Z, Wang Z (2019) Flood risk assessment in Quzhou City (China)  
543 using a coupled hydrodynamic model and fuzzy comprehensive evaluation (FCE). *Nat*  
544 *Hazards* 100(1):133-149. <https://doi.org/10.1007/s11069-019-03803-0>

545 Hossain Anni A, Cohen S, Praskievicz S (2020) Sensitivity of urban flood simulations to stor  
546 mwater infrastructure and soil infiltration. *J Hydrol* 588. [https://doi.org/10.1016/j.jhydrol.](https://doi.org/10.1016/j.jhydrol.2020.125028)  
547 [2020.125028](https://doi.org/10.1016/j.jhydrol.2020.125028)

548 Hou JW, Du YX (2020) Spatial simulation of rainstorm waterlogging based on a water  
549 accumulation diffusion algorithm. *Geomatics, Nat Hazards Risk* 11(1):71-87.

550 Hu S, Cheng X, Zhou D, Zhang H (2017) GIS-based flood risk assessment in suburban areas:  
551 a case study of the Fangshan District, Beijing. *Nat Hazards* 87(3):1525-1543. [https://doi.](https://doi.org/10.1007/s11069-017-2828-0)  
552 [org/10.1007/s11069-017-2828-0](https://doi.org/10.1007/s11069-017-2828-0)

553 Hou ZM (2019) Research on engineering case of double-loop seepage test in groundwater env  
554 ironmental impact assessment of a chemical project in Tianjin. *Ground Water* 44(04):26-  
555 28.

556 Huang GR, Wang X, Huang W (2017) Simulation of rainstorm water logging in urban area  
557 based on InfoWorks ICM model. *Water Resour Power* 35(02):66-70,60.

558 Huang M, Jin S (2019) A methodology for simple 2-D inundation analysis in urban area using  
559 SWMM and GIS. *Nat Hazards* 97(1):15-43. <https://doi.org/10.1007/s11069-019-03623-2>

560 Keifer CJ, Henry HC (1957) Synthetic storm pattern for drainage design. *J Hydraul Res*  
561 83(4):1-25.

562 Kong F, Sun S, Lei T (2021) Understanding China's urban rainstorm waterlogging and its  
563 potential governance. *Water* 13(7):891.

564 Li JZ, Li CQ, Wang FS, Zhang YW (2020) An urban storm flood model based on cellular  
565 automata. *China Rural Water and Hydropower* (11):73-76,82.

566 Li Y, Di SC, Zhu YH, Li YK, Zhang YH, Xu JM (2019) Multi-view analysis of urban flood  
567 based on multi-model coupling. *China Rural Water and Hydropower* (5):82-90.

568 Liang JH (2016) Brief analysis of application program of optimization design of waterlogging  
569 monitoring system for the Pearl River Delta cities. *Pearl River* 37(6):66-69.

- 570 Liu J, Shao W, Xiang C, Mei C, Li Z (2020) Uncertainties of urban flood modeling: Influence  
571 of parameters for different underlying surfaces. *Environ Res* 182:108929. [https://doi.org/](https://doi.org/10.1016/j.envres.2019.108929)  
572 [10.1016/j.envres.2019.108929](https://doi.org/10.1016/j.envres.2019.108929)
- 573 Meng X, Zhang M, Wen J, Du S, Xu H, Wang L, Yang Y (2019) A simple GIS-based model for  
574 urban rainstorm inundation simulation. *Sustainability* 11(10).
- 575 Peng J, Liu Y, Shen H, Xie P, Hu XX, Wang YL (2016) Using impervious surfaces to detect  
576 urban expansion in Beijing of China in 2000s. *Chin Geogr Sci* 26:229-243.
- 577 Qi W, Ma C, Xu H, Chen Z, Zhao K, Han H (2021) A review on applications of urban flood  
578 models in flood mitigation strategies. *Nat Hazards* 245. [https://doi.org/10.1007/s11069-0](https://doi.org/10.1007/s11069-021-04715-8)  
579 [21-04715-8](https://doi.org/10.1007/s11069-021-04715-8)
- 580 Quan R-S (2014) Rainstorm waterlogging risk assessment in central urban area of Shanghai b  
581 ased on multiple scenario simulation. *Nat Hazards* 73(3):1569-1585. [https://doi.org/10.1](https://doi.org/10.1007/s11069-014-1156-x)  
582 [007/s11069-014-1156-x](https://doi.org/10.1007/s11069-014-1156-x)
- 583 Rong Y, Zhang T, Zheng Y, Hu C, Peng L, Feng P (2020) Three-dimensional urban flood  
584 inundation simulation based on digital aerial photogrammetry. *J Hydrol* 584.
- 585 Seenu PZ, Venkata Rathnam E, Jayakumar KV (2019) Visualisation of urban flood inundation  
586 using SWMM and 4D GIS. *Spat Inf Res* 28(4):459-467.
- 587 Shi Y (2012) Risk analysis of rainstorm waterlogging on residences in Shanghai based on sce  
588 nario simulation. *Nat Hazards* 62(2):677-689. [https://doi.org/10.1007/s11069-012-0099-](https://doi.org/10.1007/s11069-012-0099-3)  
589 [3](https://doi.org/10.1007/s11069-012-0099-3)
- 590 Sun B, Xie SB, Wang ZY, Wu HY, Liu H (2020) Shenzhen City waterlogging prevention based  
591 on multiple LID schemes. *Yangtze River* 51(6):17-22.
- 592 Tao Cheng, Zongxue Xu, Siyang Hong, Sulin Song (2017) Flood Risk Zoning by Using 2D H  
593 ydrodynamic Modeling: A Case Study in Jinan City. *Mathematical Problems in Engineer*  
594 *ing* , Article ID 5659197, 8 pages. <https://doi.org/10.1155/2017/5659197>
- 595 Wang JJ, Wang CT, Zeng S (2020) Assessment of urban drainage capacity and waterlogging  
596 risk based on scenario simulation. *China Water & Wastewater* 36(17):115-120.
- 597 Wang SJ (2018) Evaluation of drainage capacity of urban drainage network based on  
598 infoworks ICM. *J Green Sci Technol* (18):156-159.
- 599 Wang XY, Zhou Y, Yu JN (2020) Evolution of green infrastructure layout and waterlogging  
600 risk assessment based on cellular automata simulation of urban expansion: a case study of  
601 Wuhan City. *Landsc Archit* 27(11):50-56.
- 602 Wang Y, Zhou XW (2018) Application of InfoWorks ICM in control of urban waterlogging in  
603 mountainous and hilly cities. *China Water & Wastewater* 34(19):118-123.
- 604 Xia J, Zhang Y, Ling CM, Liu J (2018) Review on urban storm water models. *Eng J Wuhan*  
605 *Univ* 51(2):95-105.
- 606 Xu B, Lei XH, Wang H, Kang AQ (2019) Research on urban flooding simulation in a coastal  
607 city based on SWMM model. *Journal of China Institute of Water Resources and*  
608 *Hydropower Research* 17(3):211-218.
- 609 Yin J, Ye M, Yin Z, Xu S (2015) A review of advances in urban flood risk analysis over China.  
610 *Stoch Environ Res Risk Assess* 29:1063-1070.
- 611 Yu H, Zhao Y, Fu Y, Li L (2018) Spatiotemporal variance assessment of urban rainstorm  
612 waterlogging affected by impervious surface expansion: a case study of Guangzhou,  
613 China. *Sustainability* 10(10):3761.

614 Zhu X, Zhou B, Qiu X, Zeng Y, Ren W, Li S, Wang Y, Wang X, Jin Y (2019) A dynamic impact  
615 assessment method for rainstorm waterlogging using land-use data. *J Integr Environ Sci*  
616 16(1):163-190.

617

618 **Figure legends**

619 **Fig. 1** Geographical location of Runcheng in the south of Kunming

620 **Fig. 2** Underlying surfaces in the study area in 2012 and 2020

621 **Fig. 3** Rainfall curve measured at the Wuda Village 816 site in the southern part of Kunming

622 **Fig. 4** Diagram of simulated flooding depths at the Wuda Village 816 site in the southern part  
623 of Kunming

624 **Fig. 5** Simulated diagram of accumulated water at the intersection of Guangfu and Qianwei  
625 West Roads

626 **Fig. 6** Simulated rainfall patterns for the 1-, 2-, 3-, 5-, and 10-year return periods

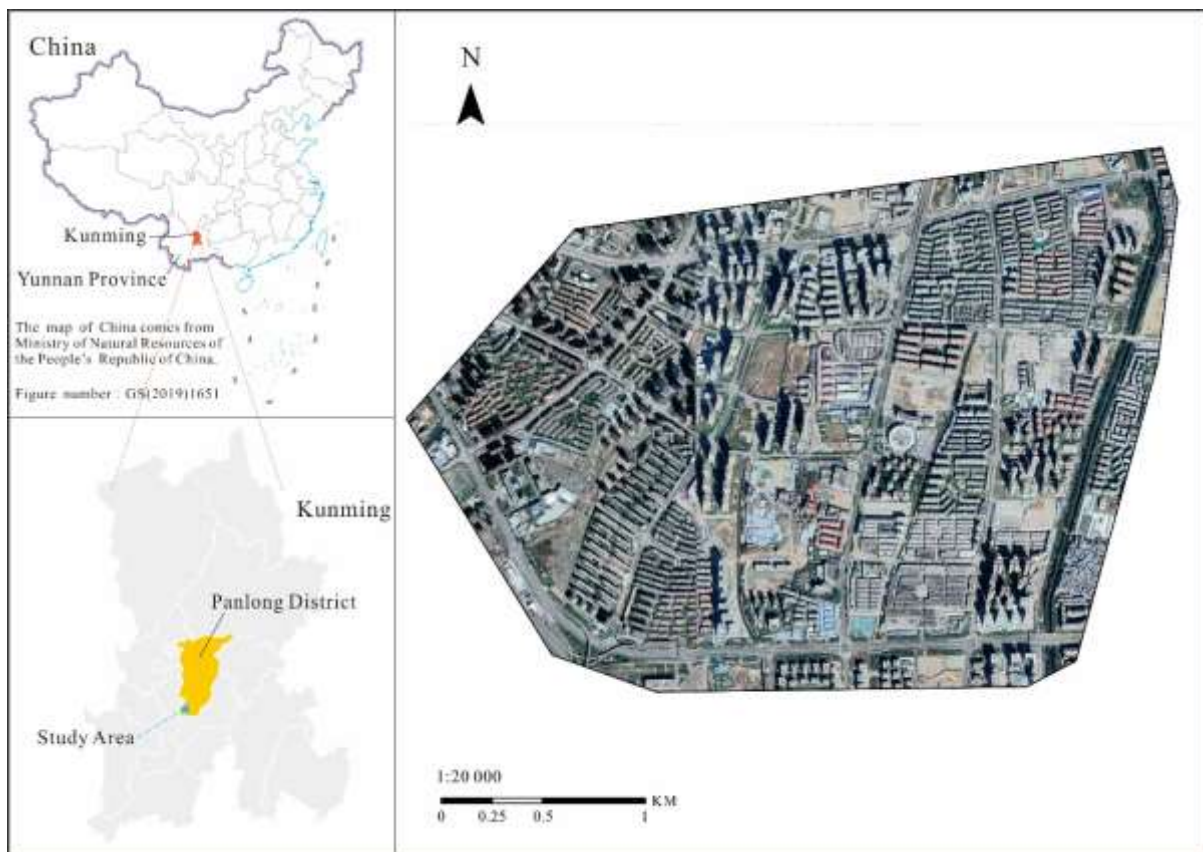
627 **Fig. 7** Simulated flood risks for the 1-, 2-, 5-, and 10-year return period rainfall

628 **Fig. 8** Flood risks for 30–60% permeable surfaces

629 **Fig. 9** Flood risks at different surface permeabilities

630 **Fig. 10** Variations in total flood risk for different surface permeabilities

631



632

633 **Fig. 1** Geographical location of Runcheng in the south of Kunming

634

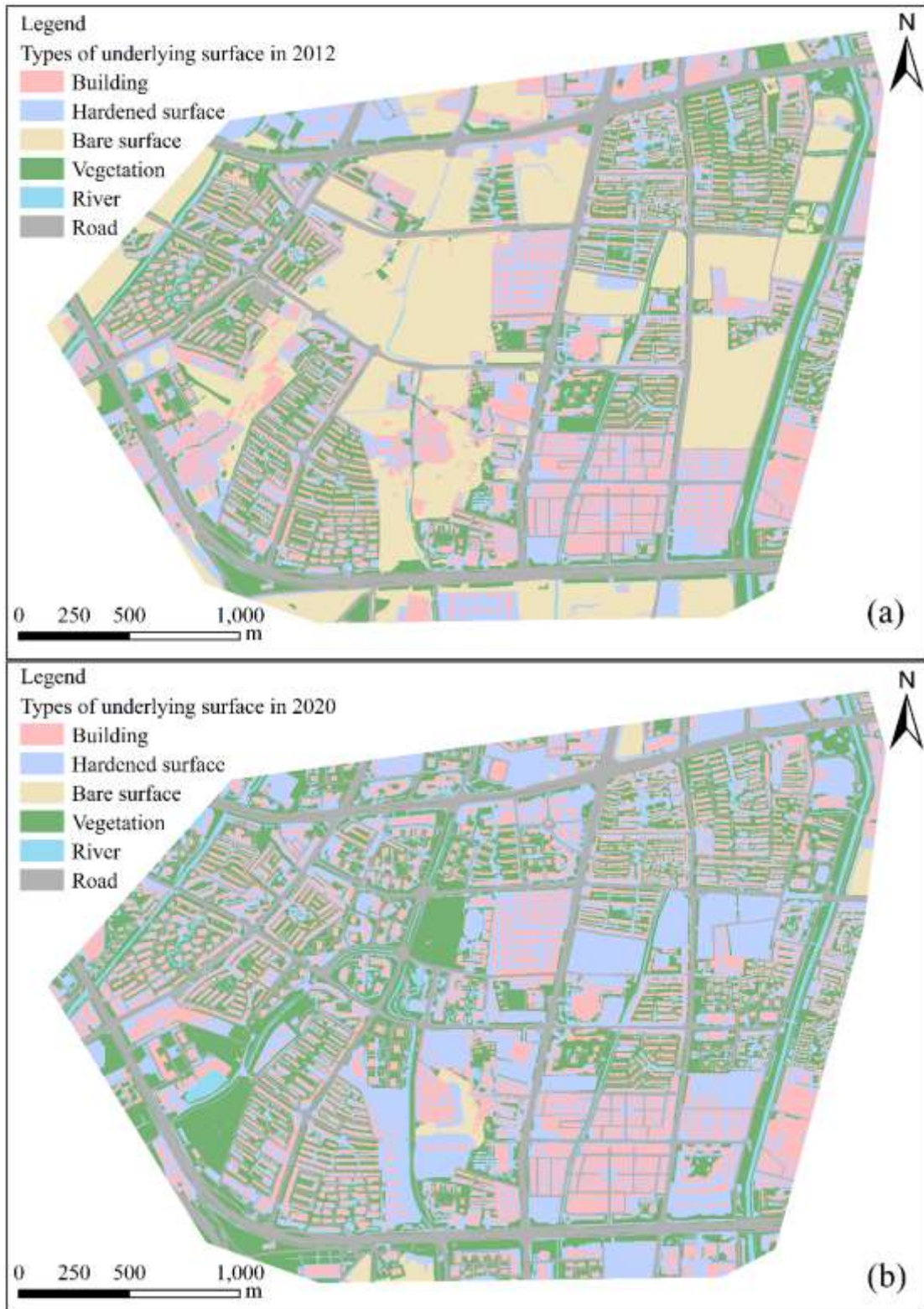
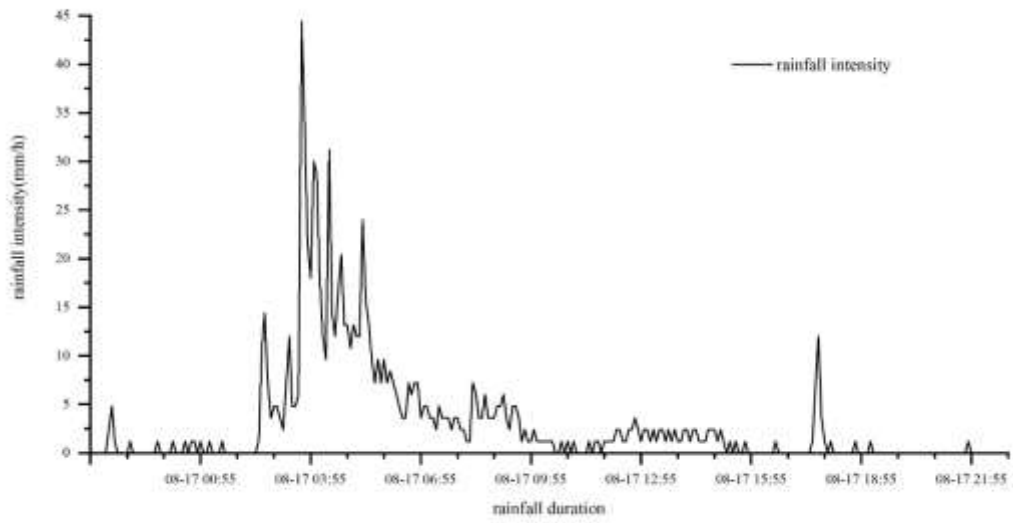


**Fig. 2** Underlying surfaces in the study area in 2012 and 2020

635  
636  
637

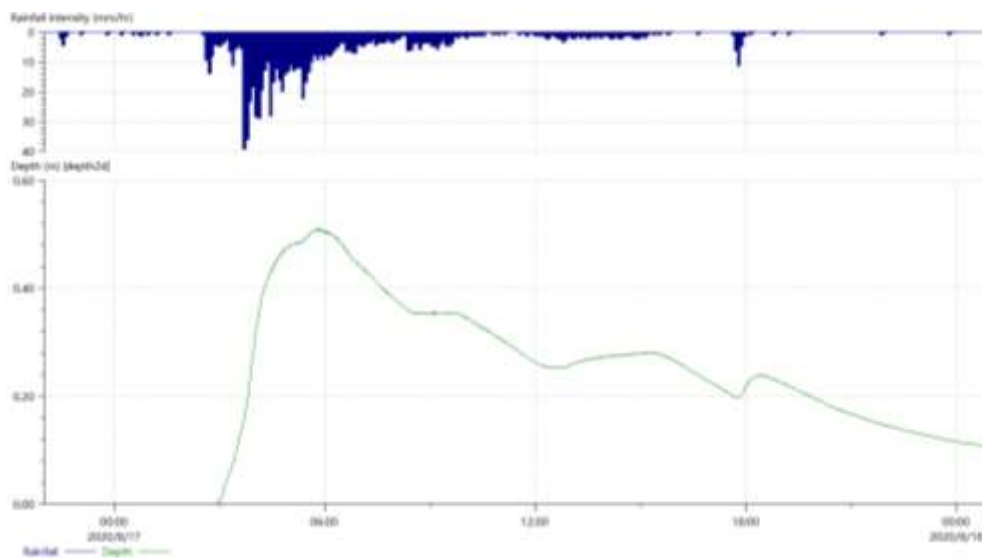


638

639

640

**Fig. 3** Rainfall curve measured at the Wuda Village 816 site in the southern part of Kunming

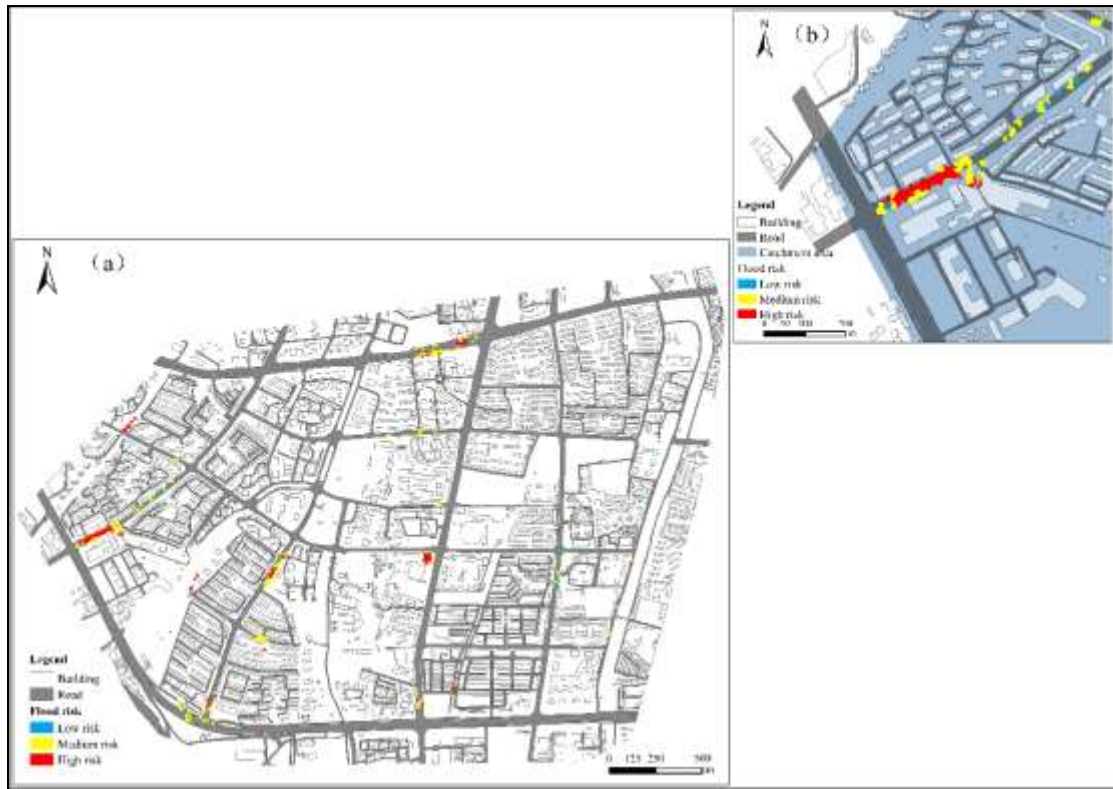


641

642

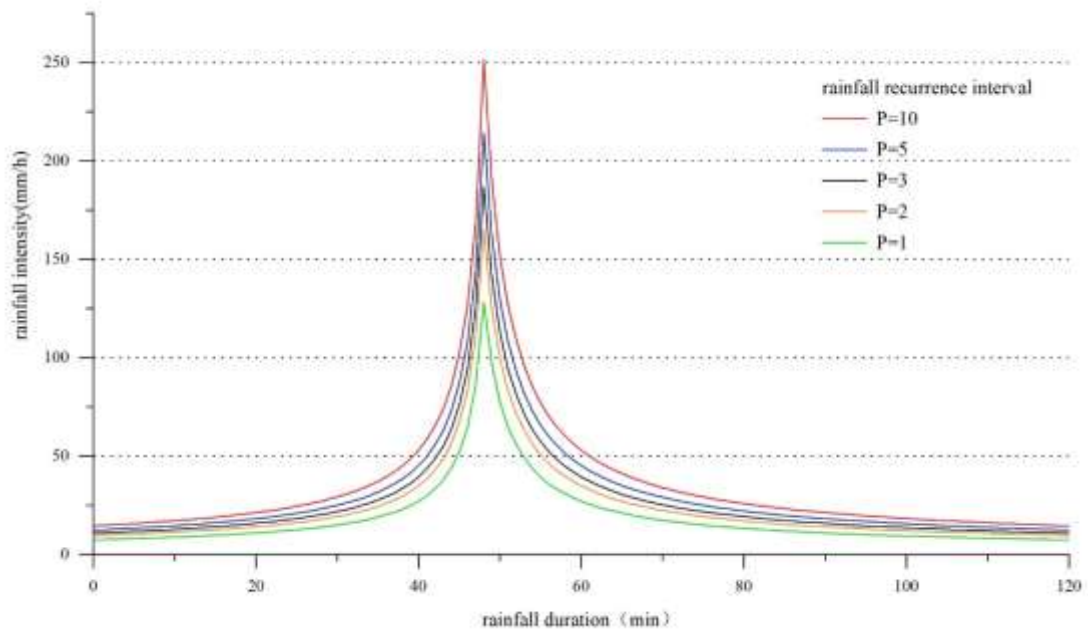
643

**Fig. 4** Diagram of simulated flooding depths at the Wuda Village 816 site in the southern part of Kunming



644  
645  
646  
647

**Fig. 5** Simulated diagram of accumulated water at the intersection of Guangfu and Qianwei West Roads



648  
649

**Fig. 6** Simulated rainfall patterns for the 1-, 2-, 3-, 5-, and 10-year return periods

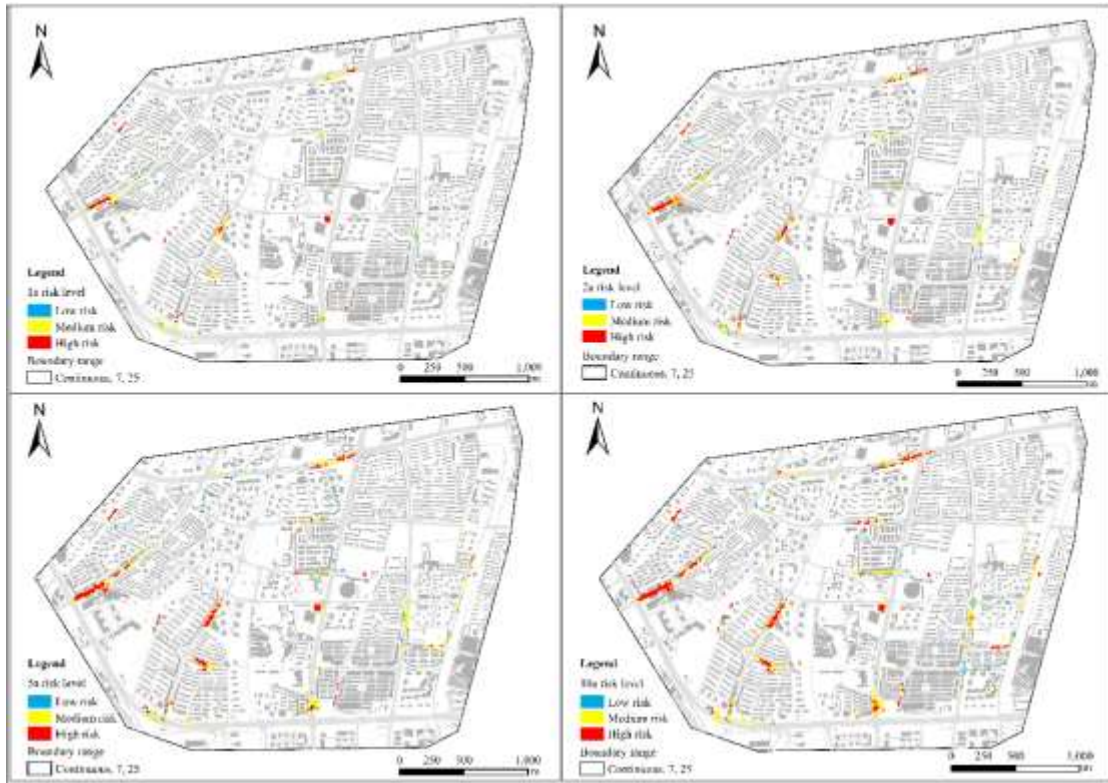


**Fig. 7** Simulated flood risks for the 1-, 2-, 5-, and 10-year return period rainfall

650  
651  
652

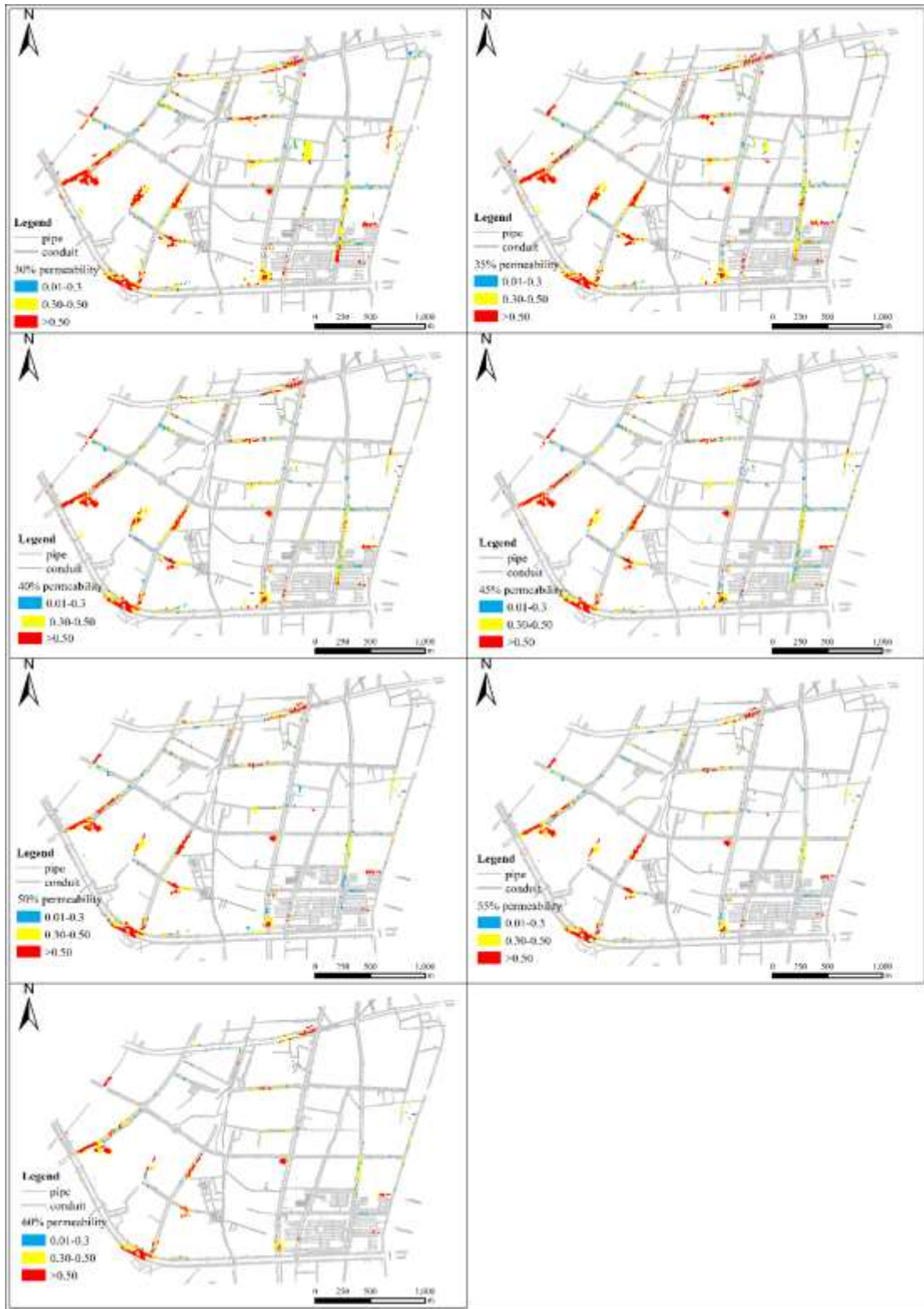


**Fig. 8** Flood risks for 30–60% permeable surfaces

653  
654  
655

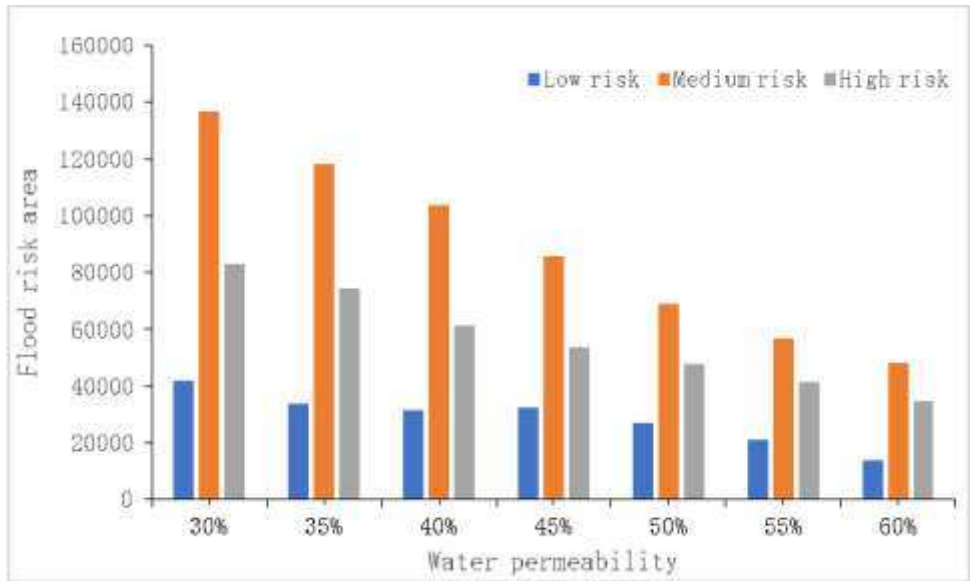


**Fig. 9** Flood risks at different surface permeabilities

656  
657  
658

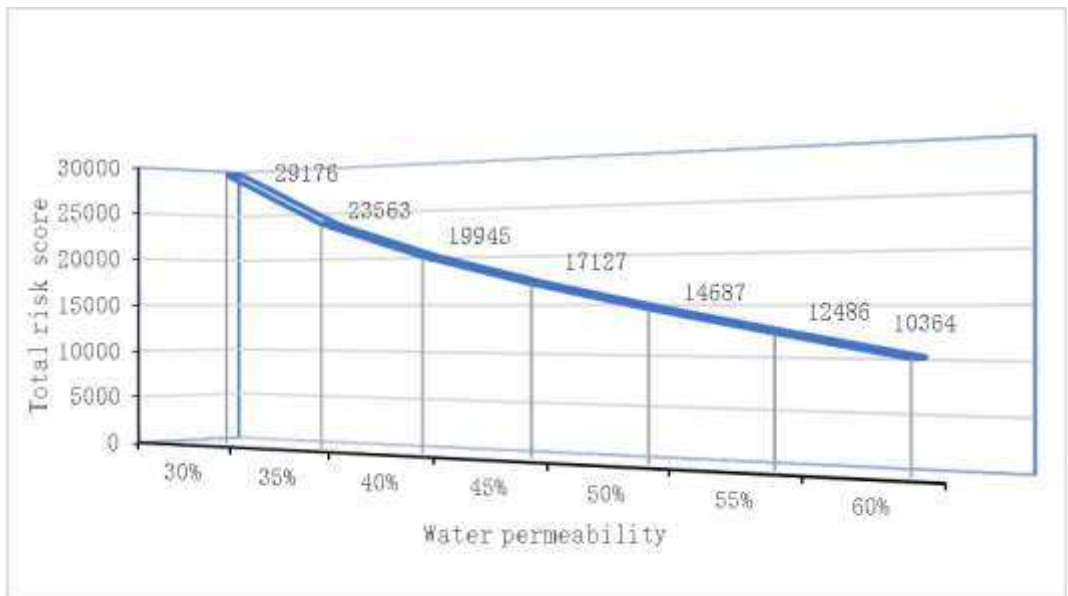


**Fig. 10** Variations in total flood risk for different surface permeabilities

659  
660  
661  
662  
663  
664  
665  
666  
667  
668  
669  
670  
671  
672

**Table legends**

**Table 1.** Data list

**Table 2.** Runoff and concentration coefficients

**Table 3.** Measured and simulated underground seepage rates

**Table 4.** Measured and simulated bare groundwater permeability values

**Table 5.** Attenuation coefficients (k) of green land and bare land and their corresponding NSE values

**Table 6.** Flood risk classifications

**Table 7.** Risk areas and their proportions in the 2020 years flood simulation

**Table 8.** Permeabilities and risk areas of the different underlying surfaces

673

**Table 1. Data list**

Data type	Data content
Geophysical data of rainwater and sewage drainage pipeline	Inspection well coordinate, elevation, pipe position, pipe diameter, pipe bottom elevation
Rainfall data	Measured rainfall data collected from a rain gauge near Runcheng area in the south of Kunming
Historical waterlogging prone point information	Including the depth, time, and scope of ponding
Remote sensing image data	Image data of Kunming City in 2012 and 2020, from Google Map, 0.5 × 0.5 m resolution ratio
Digital elevation model data	Ground elevation point data

674

675

**Table 2. Runoff and concentration coefficients**

Underlying surface type	Runoff generation model	Fixed runoff coefficient	Initial infiltration rate	Steady seepage rate	Decay rate	Confluence model	Manning coefficient
Road	Fixed	0.9	-	-	-	SWMM	0.015
Building	Fixed	0.9	-	-	-	SWMM	0.015
Vegetation	Horton	-	227	110	2.0	SWMM	0.200
Bare surface	Horton	-	77	46	2.5	SWMM	0.200
Hardened surface	fixed	0.8	-	-	-	SWMM	0.040
River	fixed	1.0	-	-	-	SWMM	0.002

676

677

**Table 3. Measured and simulated underground seepage rates**

Time (h)	Measured infiltration rate (mm/h)	$f_o$ (initial infiltration rate(mm/h))	$f_c$ (steady infiltration rate(mm/h))	$f_1$ ( $k=1$ )	$f_2$ ( $k=1.5$ )	$f_3$ ( $k=2$ )	$f_4$ ( $k=2.5$ )	$f_5$ ( $k=3$ )
0:05:22	227.75	227	110	216.98	212.31	207.83	203.55	199.46
0:11:50	189.01	227	110	206.05	197.03	188.86	181.45	174.74
0:18:56	172.15	227	110	195.33	182.88	172.24	163.15	155.39
0:27:47	138.11	227	110	183.63	168.41	156.34	146.76	139.16
0:35:33	157.37	227	110	174.69	158.10	145.77	136.60	129.78
0:43:15	158.74	227	110	166.90	149.68	137.67	129.29	123.45
0:52:27	132.85	227	110	158.81	141.52	130.36	123.15	118.49
1:01:37	133.34	227	110	151.89	135.07	125.00	118.97	115.37
1:08:55	133.95	227	110	147.09	130.88	121.76	116.62	113.72
1:18:35	126.44	227	110	141.57	126.40	118.52	114.42	112.30
1:24:08	110.11	227	110	138.78	124.27	117.08	113.51	111.74

678

679

**Table 4. Measured and simulated bare groundwater permeability values**

Time (h)	Measured infiltration rate (mm/h)	$f_o$ (initial infiltration rate(mm/h))	$f_c$ (steady infiltration rate(mm/h))	$f_1$ ( $k=1$ )	$f_2$ ( $k=1.5$ )	$f_3$ ( $k=2$ )	$f_4$ ( $k=2.5$ )	$f_5$ ( $k=3$ )
0:07:00	77.36	77	46	73.17	71.44	69.82	68.30	66.88
0:19:39	52.01	77	46	68.34	64.96	62.102	59.67	57.60
0:30:13	57.83	77	46	64.73	60.56	57.32	54.80	52.84
0:41:55	52.23	77	46	61.41	56.87	53.66	51.40	49.81

0:54:52	47.19	77	46	58.42	53.86	50.97	49.15	47.99
1:08:04	46.29	77	46	56.10	51.77	49.29	47.88	47.07
1:21:10	46.65	77	46	54.12	50.16	48.13	47.09	46.55

680

681 **Table 5.** Attenuation coefficients ( $k$ ) of green land and bare land and their corresponding NSE  
682 values

NSE	e1 (k=1)	e2 (k=1.5)	e3 (k=2)	e4 (k=2.5)	e5 (k=3)
Green land	0.49	0.84	0.85	0.74	0.60
Bare land	0.06	0.57	0.74	0.77	0.74

683

684 **Table 6.** Flood risk classifications

Ponding depth (m)	0–30 min	More than 30 min
0.15–0.30 m	Low risk	Medium risk
0.30–0.50 m	Medium risk	High risk
More than 0.5 m	High risk	High risk

685

686 **Table 7.** Risk areas and their proportions in the 2020 years flood simulation

Risk level	Area (m <sup>2</sup> )	Percentage of risk area in total area
Low risk	38,314.325	15%
Medium risk	140,484.422	53%
High risk	84,382.154	32%

687

688 **Table 8.** Permeabilities and risk areas of the different underlying surfaces

Number	Proportion of permeable area of underlying surface	Low risk area (m <sup>2</sup> )	Medium risk area (m <sup>2</sup> )	High risk area (m <sup>2</sup> )	Total risk area (m <sup>2</sup> )	Total risk score
1	30%	41,751	136,495	82,959	261,205	29,176
2	35%	33,592	118,283	74,602	226,477	23,563
3	40%	31,363	103,728	61,224	196,315	19,945
4	45%	32,236	85,551	53,546	171,333	17,127
5	50%	27,030	69,119	47,871	144,020	14,687
6	55%	21,279	56,998	41,672	119,949	12,486
7	60%	14,052	48,351	34,528	96,931	10,364

689

# Figures

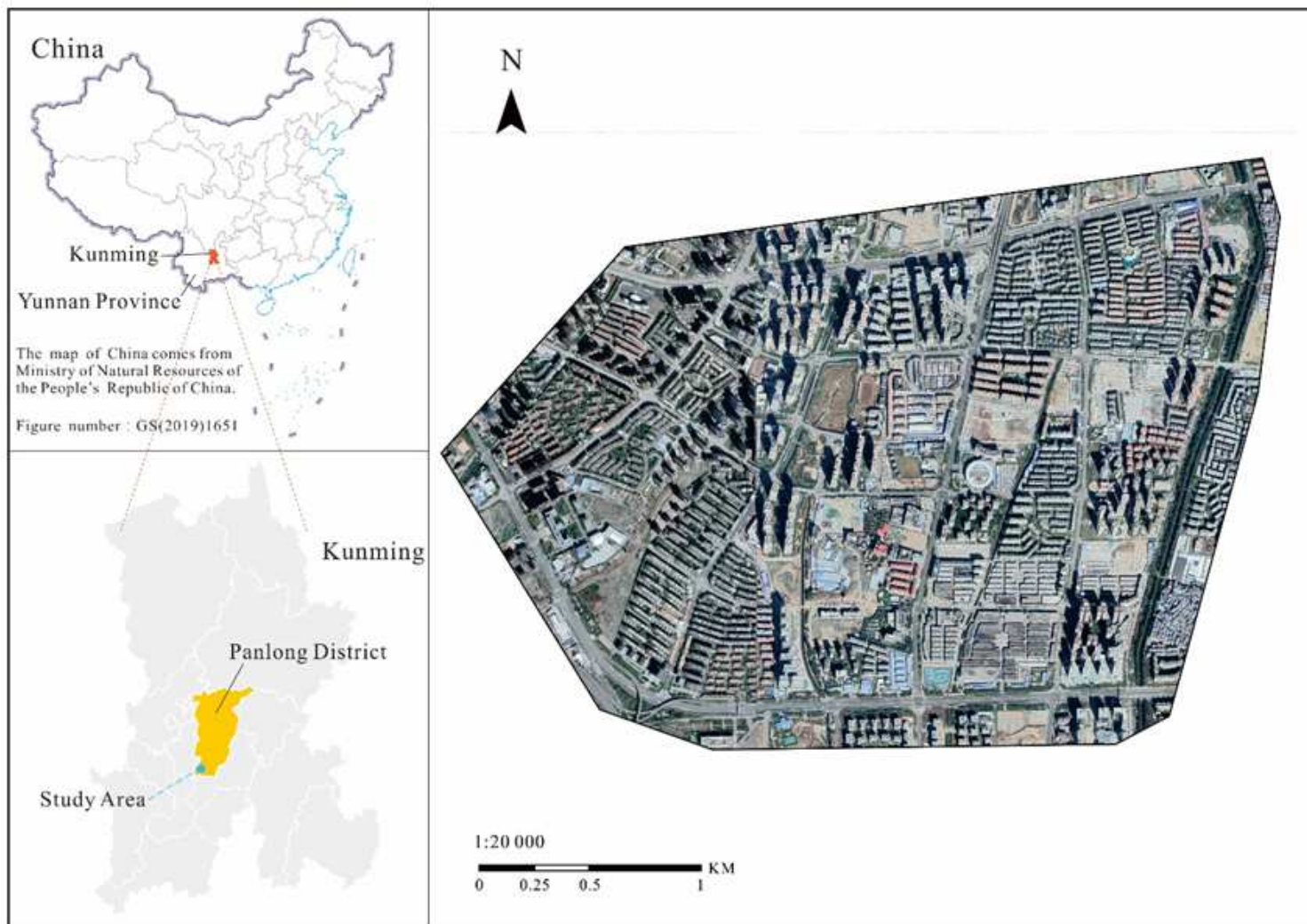


**Figure 1**

Geographical location of Runcheng in the south of Kunming Note: The designations employed and the presentation of the material on this map do not imply the expression of any opinion whatsoever on the part of Research Square concerning the legal status of any country, territory, city or area or of its authorities, or concerning the delimitation of its frontiers or boundaries. This map has been provided by the authors.



**Figure 2**

Underlying surfaces in the study area in 2012 and 2020 Note: The designations employed and the presentation of the material on this map do not imply the expression of any opinion whatsoever on the part of Research Square concerning the legal status of any country, territory, city or area or of its authorities, or concerning the delimitation of its frontiers or boundaries. This map has been provided by the authors.

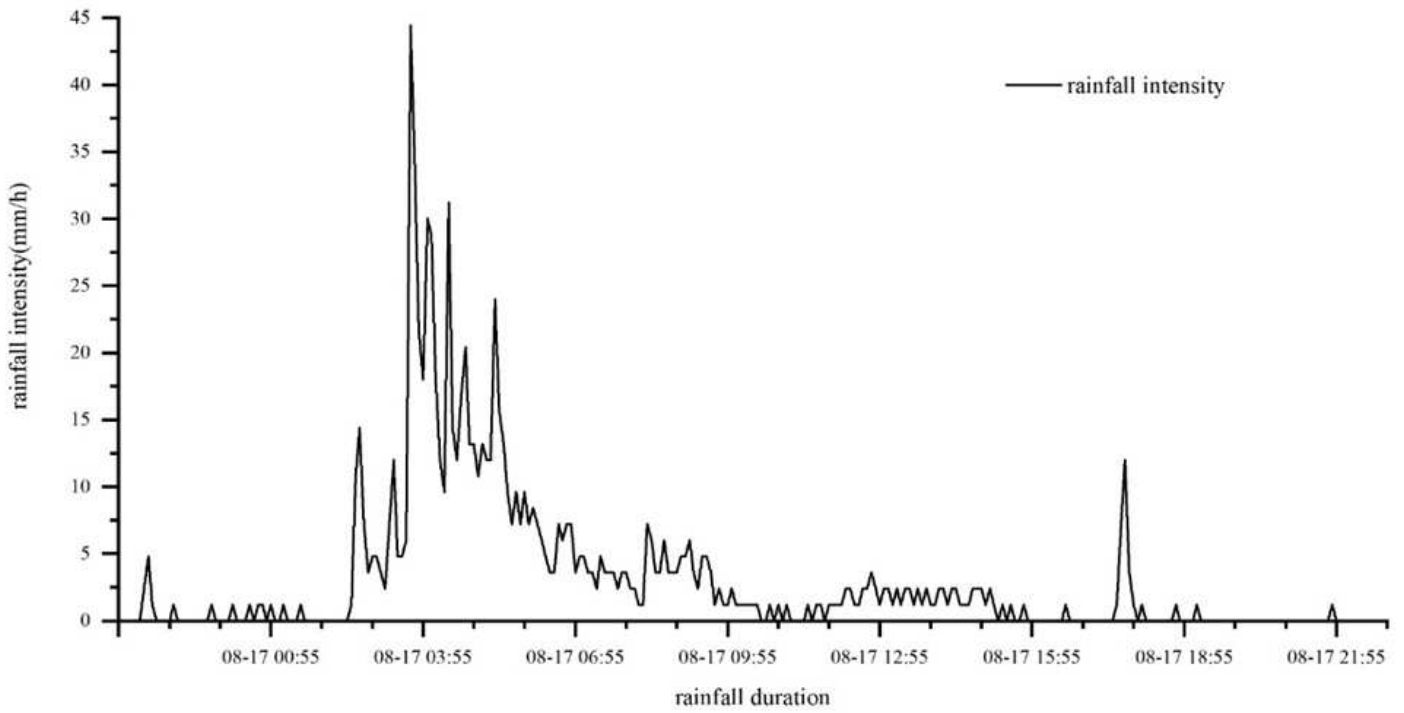


**Figure 3**

Rainfall curve measured at the Wuda Village 816 site in the southern part of Kunming

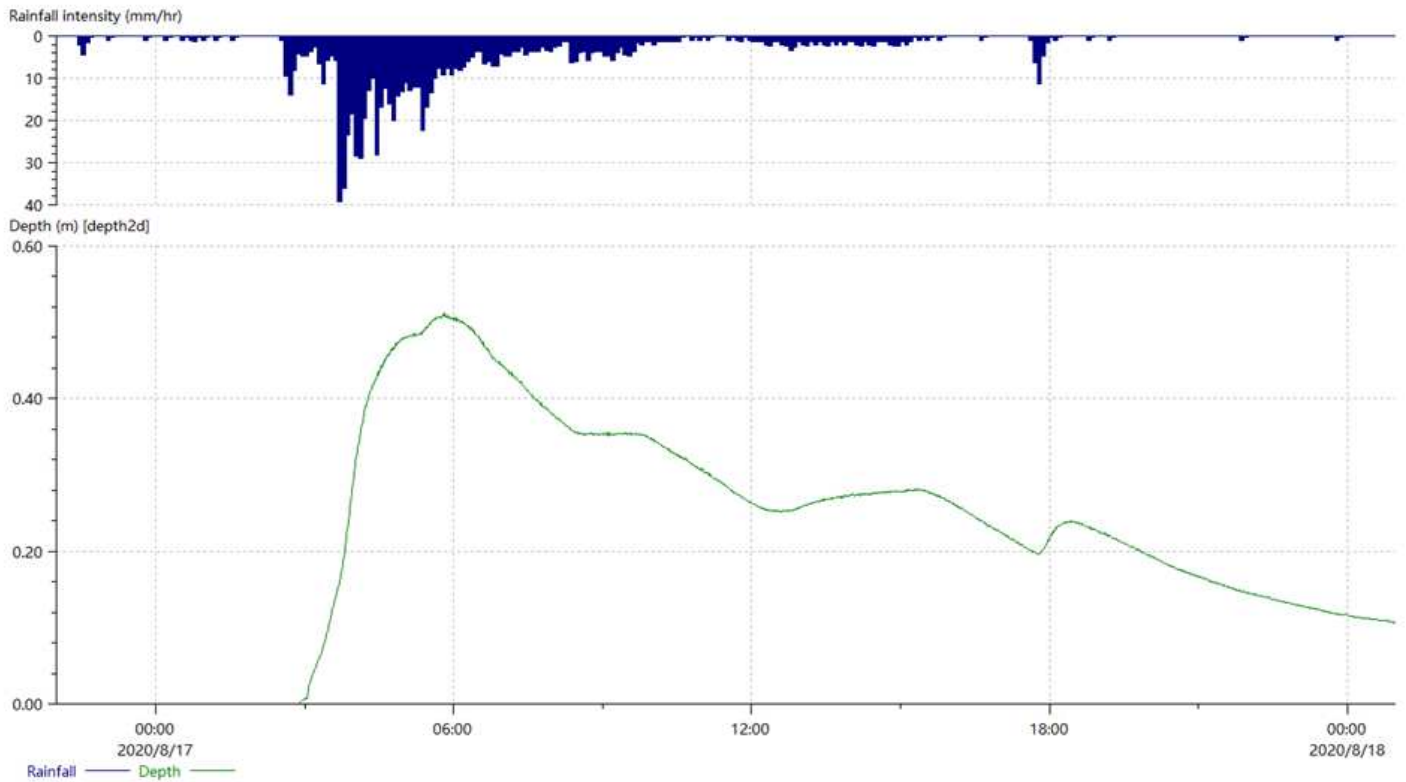


**Figure 4**

Diagram of simulated flooding depths at the Wuda Village 816 site in the southern part of Kunming

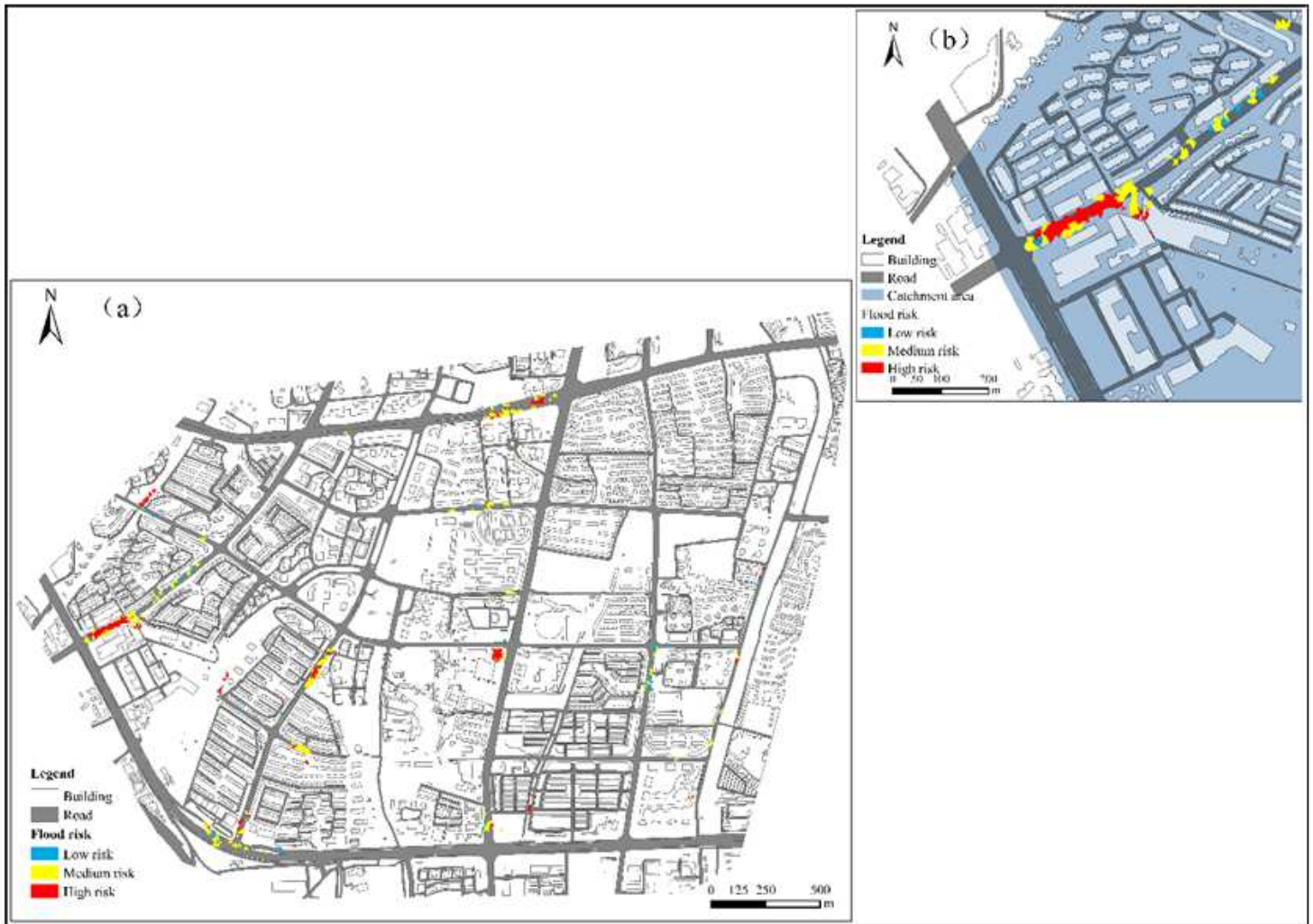
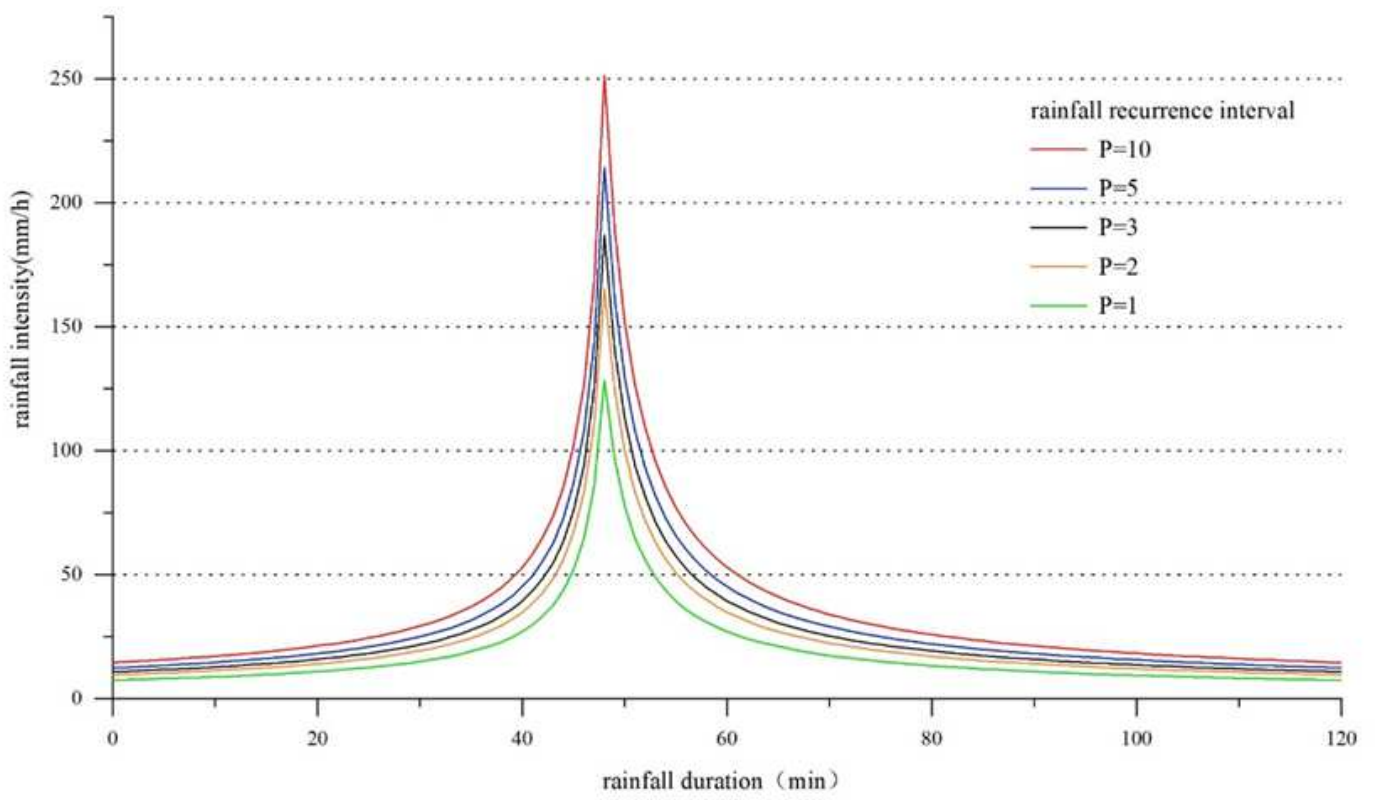


Figure 5

Simulated diagram of accumulated water at the intersection of Guangfu and Qianwei West Roads Note: The designations employed and the presentation of the material on this map do not imply the expression of any opinion whatsoever on the part of Research Square concerning the legal status of any country, territory, city or area or of its authorities, or concerning the delimitation of its frontiers or boundaries. This map has been provided by the authors.



**Figure 6**

Simulated rainfall patterns for the 1-, 2-, 3-, 5-, and 10-year return periods

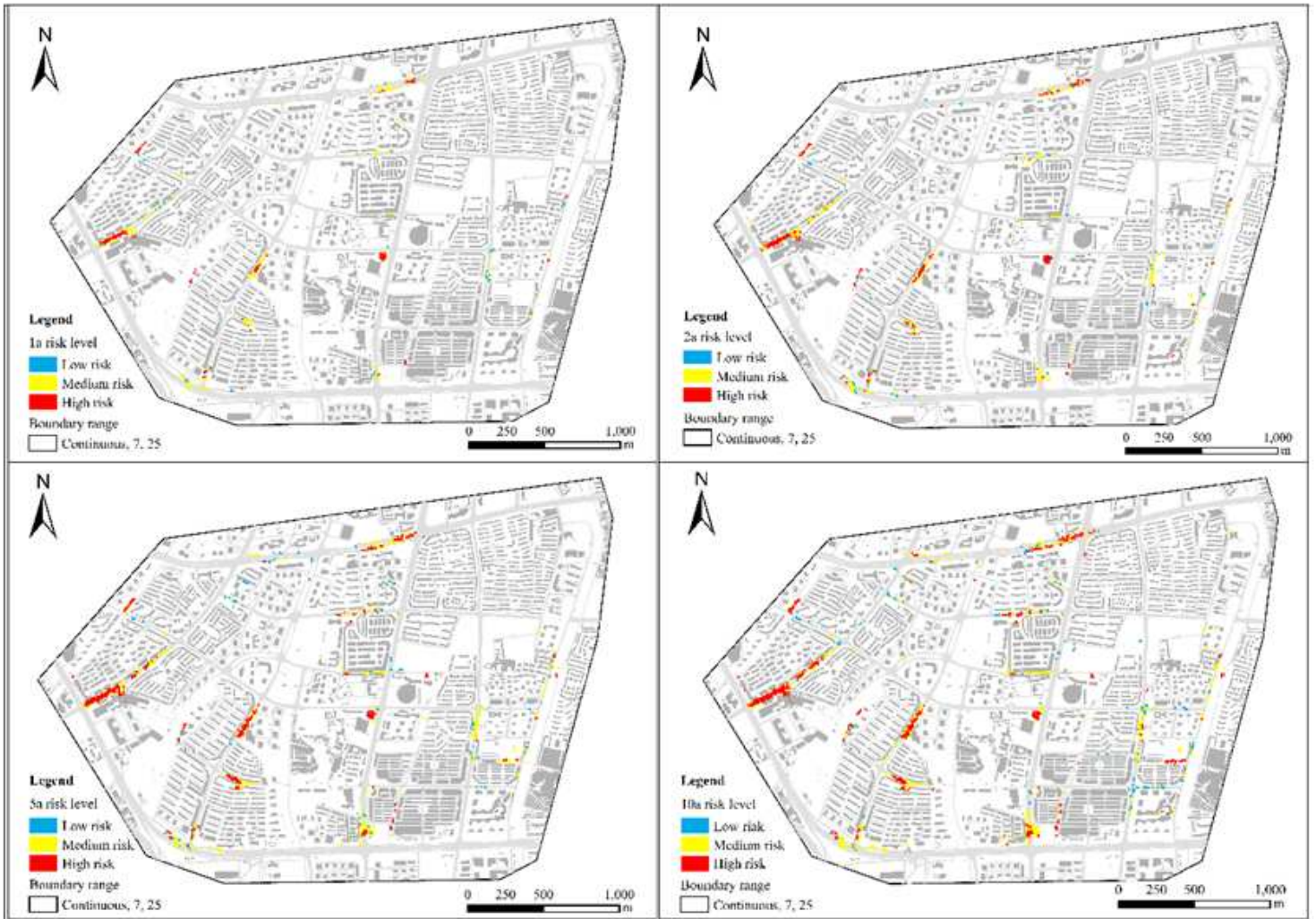


**Figure 7**

Simulated flood risks for the 1-, 2-, 5-, and 10-year return period rainfall. Note: The designations employed and the presentation of the material on this map do not imply the expression of any opinion whatsoever on the part of Research Square concerning the legal status of any country, territory, city or area or of its authorities, or concerning the delimitation of its frontiers or boundaries. This map has been provided by the authors.

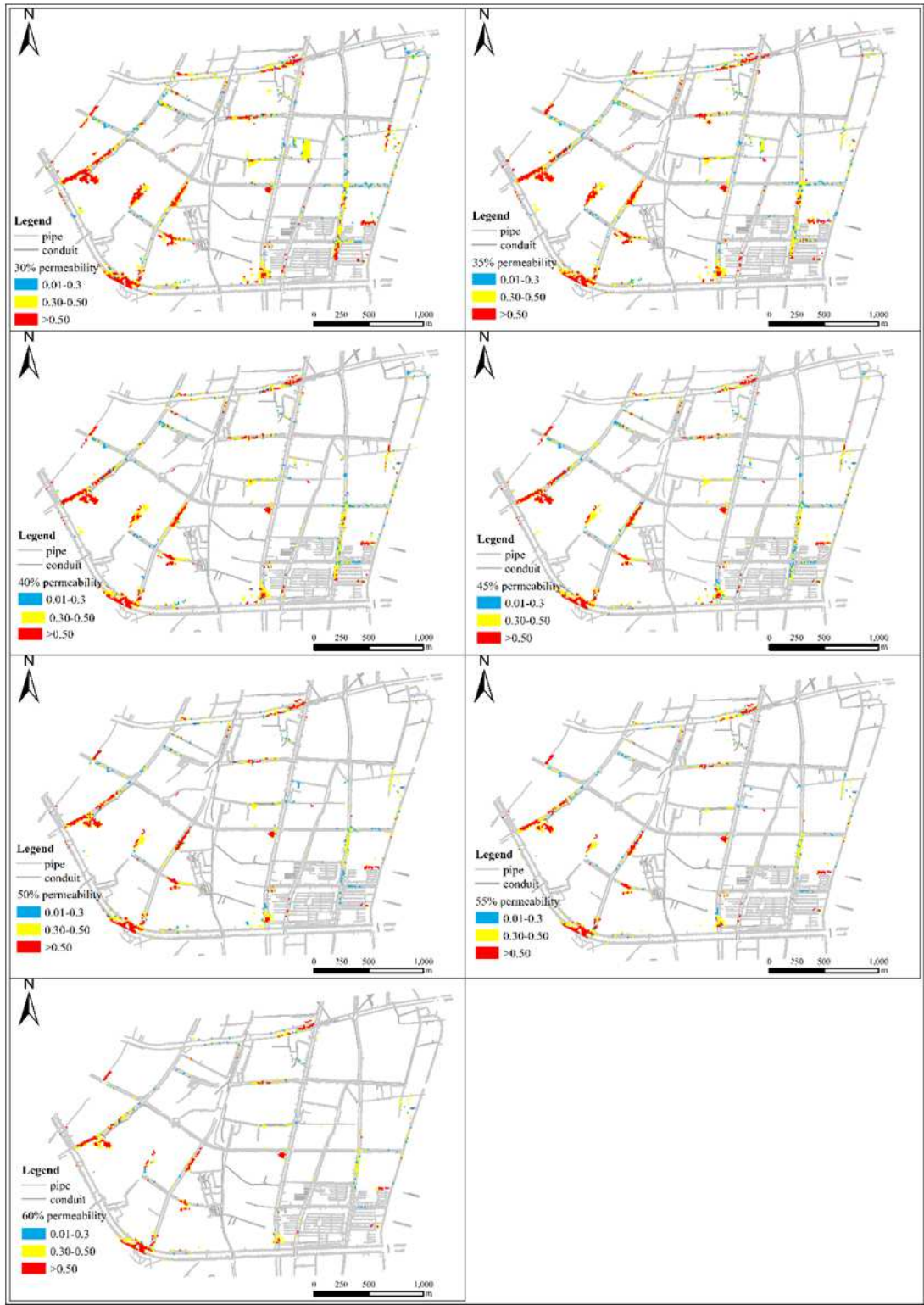


**Figure 8**

Flood risks for 30–60% permeable surfaces Note: The designations employed and the presentation of the material on this map do not imply the expression of any opinion whatsoever on the part of Research Square concerning the legal status of any country, territory, city or area or of its authorities, or concerning the delimitation of its frontiers or boundaries. This map has been provided by the authors.

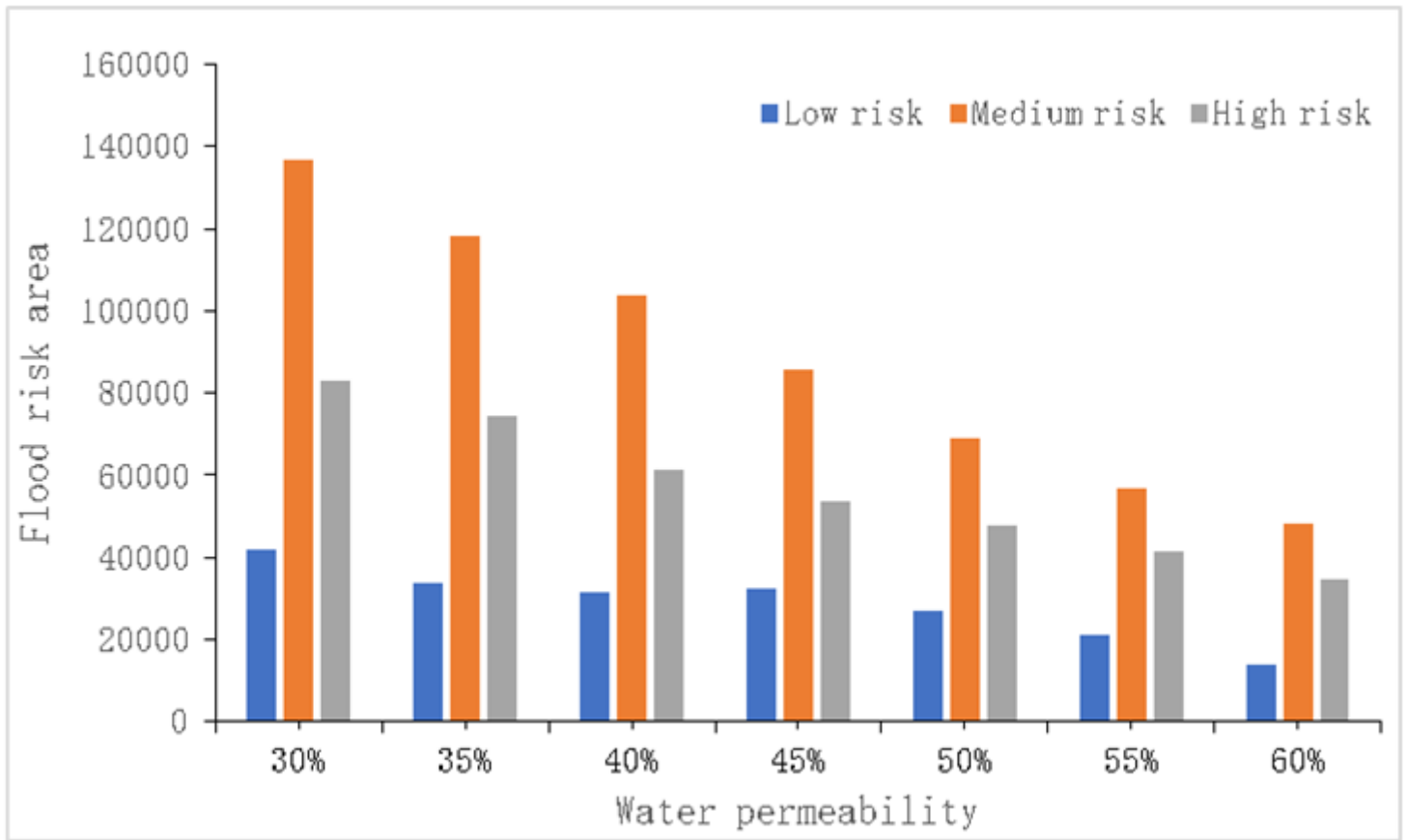


**Figure 9**

Flood risks at different surface permeabilities

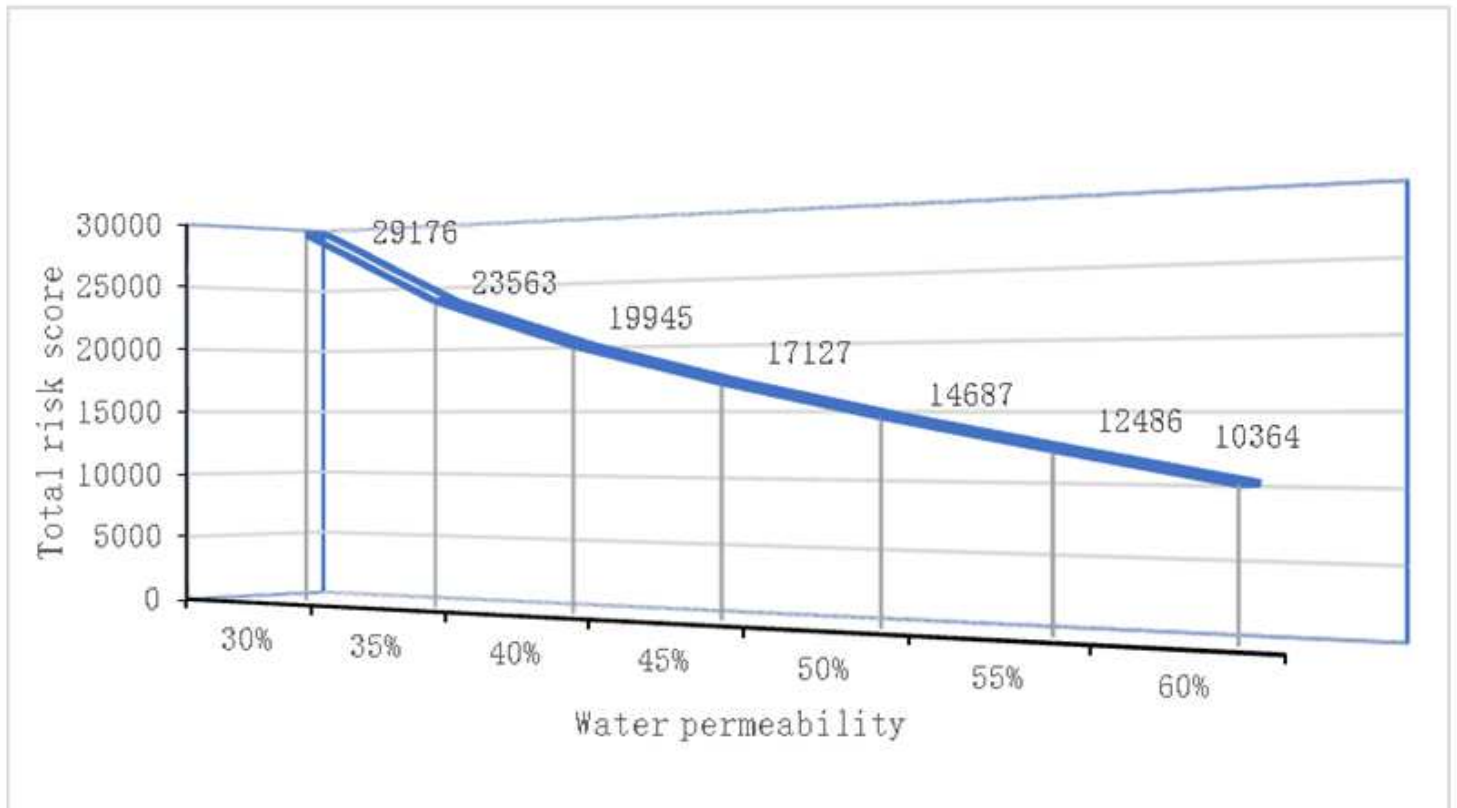


## Figure 10

Variations in total flood risk for different surface permeabilities